Thermal Properties of Materials under Pressure

Yan Zhou[1], Zuo-Yuan Dong[2,1], Wen-Pin Hsieh[3], Alexander F. Goncharov[4], and Xiao-Jia Chen[1,5*]

1. *Center for High Pressure Science & Technology Advanced Research, Shanghai 201203, China*
2. *School of Communication and Electronic Engineering, East China Normal University, Shanghai 200241, China*
3. *Institute of Earth Sciences, Academia Sinica, Nankang 11529, Taipei, Taiwan*
4. *Earth and Planets Laboratory, Carnegie Institution for Science, Washington, DC 20015, USA*
5. *School of Science, Harbin Institute of Technology, Shenzhen 518055, China*

[*]*E-mail: xjchen2@gmail.com*

Contents

Abstract: High-pressure science and technology have achieved significant progress in the past decades, enabling consistent innovation of knowledge in physical and chemical sciences, materials science, earth science, and multi-disciplinary combinations. However, measurements of thermal properties of materials under pressure and understanding of associated thermal transport mechanisms remain some of the most difficult challenges and complex topics in the high-pressure research. Thermal properties of materials are extremely important for many practical applications such as in energy conversion of devices and thermal management of electronics. However, profound understanding of thermal transport and efficient modulation methods are currently lacking. Recent breakthroughs in high-pressure experimental techniques enable *in situ* measurements of thermal conductivity at extreme pressure-temperature conditions providing a unique insight into thermal transport mechanisms and novel capabilities to realize reversible modulation of materials' thermal properties. In this Review, we discuss recent progress in thermal characterization techniques developed at high pressures, in the determination of the thermal properties of materials ranging from gases, liquids, solids to solid-solid interfaces, as well as in establishing the correlated thermal transport mechanism. Particular attention is paid to applications of high-pressure, high-temperature experimental simulation of materials at Earth's interior and the high-pressure modulations of thermal-physical properties in thermoelectrics. An outlook is also given for future theoretical and experimental investigations of high-pressure thermal properties and potential high-pressure applications on devices' thermal management techniques.
Keywords: High-pressure, thermal-physical properties, thermal conductivity, interfacial thermal conductance

1. Introduction

High pressure science and technology, as a novel and fast progressing research area, coupled with the keep-progressing achievements in characterization techniques, have been mainly exploited to simulate the high pressure environment in planetary bodies and to investigate the physical and chemical properties of materials within them.[1-10] Meanwhile, fruitful opportunities and giant scientific potential have also emerged in multi- and inter-disciplinary research area due to the improvements in versatile high-pressure techniques, which can be achieved through static and dynamic compression approaches.[3,11-24] Pressure has long been recognized as an important thermodynamic variable (besides the temperature and chemical composition) that can effectively adjust or even reversibly modulate many physical properties of materials. It, however, has also been limited or lagged in applications to relatively low pressure region for quite a long time due to previous unattainability in apparatus and techniques, until the turn of this century when the megabar (100 GPa) pressure diamond anvil cells (DAC) techniques together with a series of in-laboratory integrated characterization techniques were developed.[11,25-28] Static high-pressure

generation techniques primarily consist of Piston-cylinder pressure cell (with a pressure limit <10 GPa), multi-anvils cell (with a maximum pressure of ~90 GPa) and DAC (with a highest pressure up to ~770 GPa) apparatus.[29-34] Pressure in DAC can be conveniently determined and monitored by the fluorescence peak shift of a ruby sphere crystal (can be widely available until ~100 GPa) placed close to the sample of interest, with an uncertainty of 2-4%, or directly marked by the Raman spectra peaks collected from the near-sample diamond anvil (can be calibrated up to ~410 GPa with an uncertainty of ~15%).[35,36] Since the invention, due to its convenience and many inherent advantages, DAC has been successfully combined with various physical and chemical characterization techniques, in which a hydrostatic, stable and homogeneous compressive strain (30% or even higher) can be generated without any additional damage to the samples.[6,8,20,23,37-40] In contrast, traditional strain generation methods such as the mechanical stretching or compression of metals, or the elongation and bending of semiconductors to obtain the strain where samples sit on a flexible substrate, the strain typically can be achieved only no more than 4%;[41-44] this is far below the requirements of systematic investigation on fundamental mechanism of strain modulation. Moreover, the slippage across the sample-substrate interface or the imperfect strain transfer across different layers can introduce large uncertainties in the strain values, such as a significant scatter or even contradiction in the obtained values derived via strain-induced Raman peak shifts.[45-47] Naturally, DAC has become the broadest platform for theoretical and experimental researches from the new dimension of pressure.

In the pressure dimension, many unexpected physical properties can emerge as all materials properties will undergo changes in different high-pressure regions, and in this sense the changes normally move from the ordinary condensed-matter category to a new dense-matter physics world.[5,7-10,15-21,23,24] It is not surprising to see all the electronic, elastic, structural, magnetic, and chemical properties being altered drastically upon compression, mainly due to the interatomic bonding and orbital coupling, interlayer wave function overlap, and valence band splitting being modified.[8,15,19,20,40,48,49] The phononic or vibrational properties can also be greatly changed in many materials at high pressures, and some of them can be directly probed by *in-situ* Raman spectroscopy and Brillouin scattering techniques.[50-53] More importantly, the materials properties will be tuned by pressure across the various regimes according to conventional classification such as insulators, semiconductors and superconductors,[5,6,10,23,24,54,55] amorphous and crystalline solids, *etc*., and many new materials or phases can also be surprisingly created.[56-59] To investigate these novel physical and chemical properties under pressure, continued progresses have been achieved in high-pressure characterization techniques, including the structural, optical, electrical, magnetic and thermal characterization of samples within the DAC apparatus.[1,3,8,19,20,60] For example, the changes of lattice parameters, phase structure as well as the resultant strain induced by pressure can be accurately obtained by the combination of synchrotron X-ray diffraction (synchrotron-XRD) with DAC techniques; these developments result in great scientific progress including the recent breakthrough in exploration of metallic hydrogen and high-temperature

superconductors.[8,16,17,19] Also, the critical phenomena, phase evolution, stress state and magnitude, phonon modes and electronic bandgap which change under pressure or the equivalent strain, can be very sensitively and accurately detected experimentally by combining techniques such as *in-situ* micro-Raman, micro-photoluminescence and absorption spectroscopies with the DAC techniques.[6,7,18,20,23,40,41,61-63] Despite such tremendous achievements in high-pressure characterization of materials properties, their thermo-physical properties remain one of the most difficult properties to be reliably and accurately measured at high pressures.

Thermo-physical properties are important parameters playing crucial roles in thermal transport and thermal management; the latter has been a critical bottleneck in many high-power devices and heat exchange systems, for example, transistors and thermoelectric devices, and electronic systems in mobile-phone and computer terminals.[64-67] Thermo-physical properties discussed here are emphasized in non-metallic materials in which phonons are the major heat carriers; these properties mainly involve thermal diffusivity, thermal conductivity, heat capacity, phonon velocity, phonon mean-free-path (MFP), phonon lifetime, interfacial thermal conductance (ITC), and thermal resistance. Phonons have a large variation in their frequencies and MFPs; for bulk materials at room temperature, MFP is normally in the range of 1-100 nm which is within the microstructure scale of the bulk materials.[68] However, in micrometer-scale and even nanometer-scale samples, phonon MFP will be comparable or even limited to the sample length or width or thickness, resulting in stronger boundary scatterings and thus lowering the thermal conductivity. Concerning the aspects of common measurements and applications, thermal conductivity and ITC are the most discussed correlative thermal parameters, where thermal conductivity is significantly affected by sample thickness, width and length,[69] and also by strong point-defects or dislocation scatterings and isotope scatterings.[70] While ITC is normally related to the interfacial atomic bonding strength, atomic mixing, interfacial microstructure and interfacial roughness as well as the materials quality near the interface. Both thermal conductivity and ITC are temperature dependent parameters, varying in different temperature regions through different phonon scattering mechanisms; this makes temperature, the most often used external stimuli because of its easier availability, a useful variable to tune, modulate, and control the thermal performance of materials and devices. Besides, strain or pressure can also be used to tune the thermal conductivities of materials and ITCs at interfaces, despite this part of research is still in its early stage due to the challenges and difficulties in high-pressure thermal characterization techniques.[3,22,38,39,49,60,71-76] Thermal conductivities of some solids and liquids at pressures only up to a few GPa determined with the errors of a few percent were summarized in 1984; this includes the proposed pressure-dependent thermal transport mechanisms for alkali halides, simple metals and non-metallic liquids being theoretically described.[77] Later in 2007, the pressure dependences of thermal properties of some geophysically relevant minerals up to 10 GPa were summarized, reporting the re-examined experimental values of the thermo-physical parameters with higher accuracy determined using a contact-free laser-flash method.[14]

Recently, some theoretical and experimental studies have been performed to probe the strain or high pressure effects on thermal conductivities in a variety of materials demonstrating rich high-pressure phenomena.[3,22,38,39,49,60,74-76,78,79] For example, the thermal conductivity of solid iron at planetary core conditions up to 130 GPa and 3000 K was directly measured using pulsed laser transient heating method.[3] Knowledge of thermal-physical properties under pressure can also advance understanding of heat transport mechanism and provide useful guidelines for the tunability of thermal properties via pressure or strain method in thermal management, such as the recent breakthrough in thermal conductivity measurements of MoS_2 under pressure.[49] This Review will focus on the discussion of pressure-induced modifications in thermo-physical properties of materials, thermal transport behaviors and thermal applications under pressure ranging from ambient pressure up to hundreds of GPa.

2. Basic theory of thermal transport

Heat flux generated and transported through a material is normally described by Fourier's law of heat conduction:

$$\dot{Q} = -\kappa \nabla T, \tag{2.1}$$

where $\dot{Q}$ is the local heat flux with a unit of Wm^{-2}, κ is the thermal conductivity of material in a unit of $Wm^{-1}K^{-1}$, ∇T is the local temperature gradient through the material thickness in a unit of Km^{-1} (see schematic in Figure 1a). The Fourier's law describes how efficiently the heat can be conducted through a material from its high temperature to low temperature regions. However, in thermal characterization of various materials and practical device applications, one should take into account that besides transport through the materials, heat also has to be conducted across the interfaces of different materials (including dissimilar, epitaxial, bonded, and contact interfaces). In this case, the thermal resistance of the interface is commonly employed to evaluate the thermal transport efficiency. The thermal resistance is normally described as:

$$R = \Delta T/Q, \tag{2.2}$$

where ΔT is the temperature difference between the two surfaces (in a unit of K), and Q is the thermal energy conducted through these two surfaces area (in a unit of W). Therefore, the total thermal resistance R consists of the part along the thermal conduction path of the materials that is dependent on the thermal conductivity and thickness of the materials, as well as the thermal boundary resistance at the interface of two different materials which depends on many interfacial factors including the micro- and nano-structure, atomic bonding condition, atomic mixing, surface roughness, surface termination, contamination, and others.

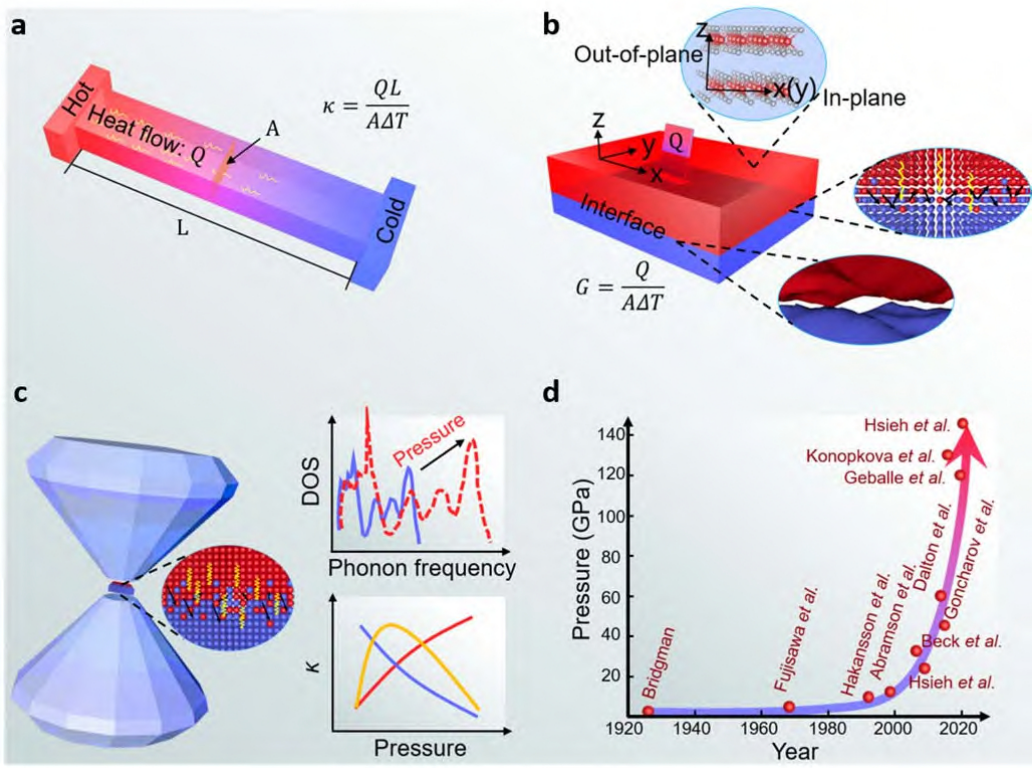

Figure 1 | Thermal transport in materials at ambient and high pressures. a | The description of thermal transport and thermal conductivity by Fourier's law of heat conduction. A, Q, and L represent the cross-sectional area, the total thermal energy of heat flow through the cross-sectional area, and the length of thermal transport, respectively. ΔT is the temperature difference from the hot to the cold terminals. The thermal conductivity is expressed as $\kappa = \frac{QL}{A\Delta T}$. **b** | The description of interfacial thermal conductance between two different materials as well as the in-plane and out-of-plane thermal conductivity. Heterointerface contact normally includes conditions of the full contact and the limited contact where some air voids are inevitably introduced during the integration; both of them normally result in an obvious temperature drop ΔT across the interface due to the mismatch of phonon scattering between the two different materials. The interfacial thermal conductance is expressed as $G = \frac{Q}{A\Delta T}$. **c** | The schematic of thermal transport at high pressures generated within a diamond anvil cell as well as the schematic evolution of phonon density of states and thermal conductivity with respect to pressure. In general, the application of pressure compresses the crystal lattice and extends the phonon frequency, thereby can promote the heat carrying ability of electrons and some phonons, bringing about the modification of the thermal conductivity under pressure (e.g., increasing trend, decreasing trend and anomalous trend). **d** | The progress in thermal conductivity measurements at high pressures. The values of pressure and year in panel **d** are taken from Refs.[3,38,39,60,115,116,137,150,189,213].

2.1. Thermal conductivity

Heat transfer ability at the macroscopic scale is characterized using thermo-physical properties such as the thermal conductivity. These thermal properties in turn are correlated to the atomic-level properties and the transport process, mainly through microscale energy carriers like phonon, electron and hole, fluid particle, photon, and so on. In non-metallic crystals such as semiconductors and some thermoelectrics, the main heat carriers are phonons. The total thermal conductivity κ of a crystal involves contributions from a lattice (phonon, κ_l) and an electronic (electron, κ_e) component, which is described by:[80]

$$\kappa = \kappa_l + \kappa_e = \sum_j \frac{1}{3} C_v v_j l_j + L\sigma_e T, \tag{2.3}$$

where C_v, and v_j are the molar heat capacity at constant volume, and the phonon group velocity of the *j*th phonon mode, respectively; l_j is the MFP of the *j*th phonon mode which can be further expressed as $l_j = v_j \tau_{p,j}$ where $\tau_{p,j}$ is the effective phonon scattering time of the *j*th phonon mode, including contributions from all scattering factors; L, σ_e, and T are the Lorenz number, electrical conductivity, and temperature, respectively. In metals, κ is dominated by κ_e owning to the large concentration of free electrons. Both electrical and thermal transport processes involve significant contribution from the free electrons in metals, mainly because the free electrons can be accelerated to a higher drift velocity with a higher energy by the electric field. Hot electrons at higher energy states can carry more thermal energy than cold electrons. The Wiedemann-Franz law ($\kappa_e = L\sigma_e T$) is traditionally used to calculate the contribution of electrons to the thermal conductivity on the basis of σ_e, where $L = (\pi^2/3)(k_B/e)^2$ is normally applied for metals (e and k_B are the electron charge and Boltzmann constant, respectively). In contrast, in semiconductors various doping levels result in much smaller σ_e, and thus smaller κ_e. Therefore, in non-metals such as the semiconductors of GaN, diamond, Si and SiC, and the thermoelectrics of Bi_2Te_3 within the operational temperature range of electronic devices applications, heat is mainly transferred through the lattice vibrations,[80] making κ_e negligible compared to κ_l. Therefore, κ_l, denoted as κ from now on in the text, will be discussed primarily in this work.

Phonons can be scattered by various mechanisms in an imperfect crystal, shortening the average distance they can travel through the lattice, *i.e.*, lowering their MFPs. Contribution of different mechanisms on phonon scattering are temperature dependent, thus resulting in a temperature-dependent thermal conductivity. Typical phonon scattering mechanisms include contributions from crystalline boundaries, lattice defects and impurities, electrons, and other phonons; below we denote them in terms of the characteristic scattering times.

(1) Phonon-boundary scattering (τ_{p-b}, see the schematic in Figure 2a): It is noted that below 10 K, scattering from the crystal boundaries (crystal size or grain size) dominates because of the finite size of the crystal,[80] especially in micro- and nanoparticles. Therefore, the thermal conductivity of an ultrathin film may be

significantly different to its bulk value due to the phonon transport hindered by increased boundary scattering. This is especially true when its thickness is close to the value of the dominant phonon MFP. For example, the dominant phonon MFP range can be suppressed to a few nanometers by defects, impurity and grain boundaries in Bi_2Te_3.[81-83] This illustrates why Bi_2Te_3 films with 20-100 nm nanostructures present a few times smaller thermal conductivity when compared to bulk and pure Bi_2Te_3 due to the suppression of long MFP phonons.[82]

(2) Phonon-impurity scattering (τ_{p-im}, see the schematic in Figure 2b): The crystal lattice can be distorted by point defects such as impurities/dopants, vacancies, and isotopes because of their different mass compared to the host atoms, therefore resulting in stronger phonon scatterings. In addition, these point defects can change the bonding between atoms. Linear defects, for example dislocations, also scatter phonons because the cores and the surrounding strain fields of these dislocations can change the crystal density and phonon group velocity, respectively.

(3) Phonon-phonon scattering (τ_{p-p}, see the schematic in Figure 2c): Inter-phonon scattering is the most significant scattering mechanism at higher temperature and is highly temperature dependent. In principle, inter-scattering processes between phonons can induce a local strain that changes the phonon velocity. Three-phonon processes are normally exploited to describe the phonon-phonon scattering and can be further divided into the Normal (N) and Umklapp (U) processes. This scattering mechanism is more complicated and has different behaviors for low temperature and high temperature conditions, as well as for longitudinal and transverse polarizations.

(4) Phonon-electron scattering (τ_{p-e}, see the schematic shown in Figure 2d): Contributions from electron scatterings sometimes also need to be considered. In general, the electron-phonon scattering term is complicated and strongly depends on the electron carrier concentration, normally resulting in a negligible strength of this scattering term.

(5) Van der Waals (vdW) scattering (τ_{vdW}): In the special case of layered materials, one crystal orientation bonded via weak vdW force limits heat transport along that crystal orientation and is partly responsible for the lower thermal conductivity observed along this direction. Therefore, an additional vdW scattering rate is added in order to simulate the extra resistance to the heat transport.[84,85] In this vdW scattering, the transmissivity between two neighbor layers contacted by vdW bonding is modelled with a simplified formulation of Prasher transmissivity,[86] while the interatomic potential is often described by a short-range one and a long-range one,[87-89] where the short-range one is typically Morse potential.

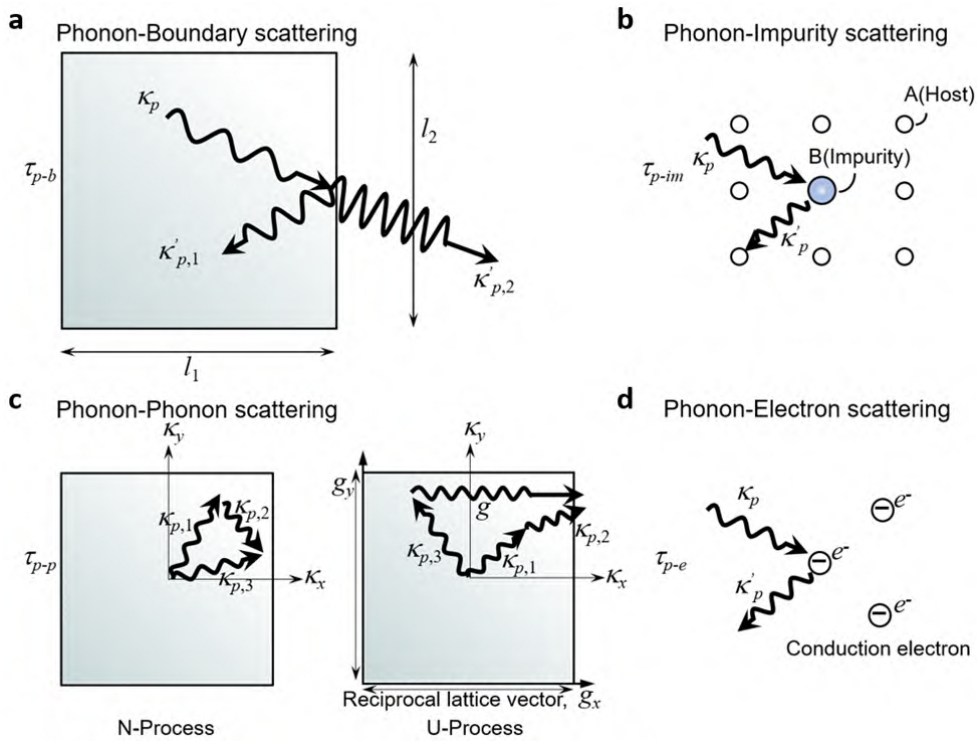

Figure 2 | Phonon scattering mechanisms. a | Phonon-boundary scattering, τ_{p-b}, where l_1 and l_2 are the crystal linear dimensions. **b** | Phonon-impurity scattering, τ_{p-im}. **c** | Phonon-phonon scattering, τ_{p-p}, where N-Process represents the Normal process and U-Process represents the Umklapp process. **d** | Phonon-electron scattering, τ_{p-e}. Note that k_p, $k_{p,1}$, $k_{p,2}$, and $k_{p,3}$ represent incident phonons, while k'_p, $k'_{p,1}$ and $k'_{p,2}$ represent scattering phonons, and the different subscripts mean the phonons with different momentums. Panels **a-d** are adapted with permission from Ref.[69] ©Springer Nature Publishers Limited.

2.2. Interfacial thermal conductance

When heat transfers across heterogeneous material interfaces, an abrupt temperature drop may occur at interfaces, forming a significant bottleneck for the thermal transport. The efficiency of this interfacial heat transfer is quantified by the interfacial thermal conductance (ITC, it is normally expressed by the symbol of G) which physically correlates the heat flux to the temperature drop at the interface via formula of $G = \dot{Q}/\Delta T$, where $\dot{Q}$ is the heat flux (in units of Wm^{-2}) across the interface area and the units of G is $Wm^{-2}K^{-1}$ (see the schematic in Figure 1b). The first quantitative experimental report on G was conducted by Kapitza who measured the interfacial thermal conductance between a solid copper and liquid helium in 1941, which is later also termed as "Kapitza conductance".[90] Mathematically, G is the inverse of thermal boundary resistance (TBR). On the one hand, ITC is a critical thermal parameter that governs the ability or efficiency of thermal energy dissipation in a wide range of devices for applications and technologies, such as high power and high frequency transistors, high frequency photodiodes, high power light emitting

diodes, and phase change memory devices.[64,65,91-94] On the other hand, low ITC also implies that the equivalent ultrathin interfacial material formed at the heterogeneous interface has a low thermal conductivity which is desirable for applications in thermoelectric materials, thermal barrier coatings, etc.[67,95-98] All these various applications require fundamental knowledge of ITC related thermal-physical theories.

Better understanding of the interfacial thermal transport mechanisms following Kapitza's groundbreaking work have been be achieved by focusing investigations on its interplay relationship with interfacial properties and the near-interface material properties.[64,65,99-107] In terms of solid-solid interfaces, the main controlling factors of ITC are (1) the phonon dispersion and density of states for energy carriers in the respective materials and the near-interface materials region; (2) the interface quality, *i.e.* the interfacial imperfection (ideally perfect smooth interfaces are almost never realized in realistic situations), such as disorder, amorphous, microstructural roughness and atomic mixing which can alter materials vibrational properties and the strength of the interfacial atomic interactions; (3) temperature. In this Review, we first introduce the conceptual theory of ITC at the interfaces, together with the experimental work that has challenged this theoretical knowledge. Then we present some of recent technological and theoretical achievements in understanding of mechanisms of ITC and its modulation explored in a new pressure dimension.

2.3. Thermal transport mechanism under pressure

Application of extreme pressure profoundly affects the phononic and vibrational properties by changing the elastic constants, sound velocities, phonon lifetimes, phonon densities of states, and interface bonding stiffness, etc.; these are closely related to the phonon transport (equivalently, thermal transport) properties of materials. Upon compression, various pressure dependences of thermal conductivities are reported, making the detailed mechanism of thermal transport modulated by pressure particularly complicated (Figure 1c). In general, the pressure dependences of κ are classified into increasing, decreasing, independent and anomalous trends. Normally, on the one hand, the strain generated by pressure will enhance the atomic interaction and compact the intralayer and interlayer bonds, heavily modify the phonon dispersions, thus leading to the phonon velocities being greatly enhanced, which means a drastic increase in κ. Such enhancement in κ with respect to pressure in some cases is nonlinear. This is found to arise from the combined effects of decreased phonon relaxation time coupled with increased phonon group velocity.[108] The electronic thermal conductivity discussed in previous section largely depends on the electronic conductivity and thus can have several orders of magnitude increase. However, it is still negligible compared with the value of lattice thermal conductivity in non-metals. On the other hand, pressure-induced phonon anharmonicity and phonon softening are thought to be as the main mechanism for the decreasing trend of κ upon compression.[109] In accord with this, first-principles calculations reveal that the decreased κ under pressure is mainly ascribed to the stronger third anharmonic interaction, the large mass ratio and the significant acoustic-optical frequency gap.[110]

For the pressure independent trend of κ, the strong electronic correlation effects driven by the electronic topological transition are presently thought as the main reason.[111] As to the anomalous trend of κ, several different mechanisms have been put forward: (1) In the case of anomalously decreased pressure dependence of κ, the failure of three-phonons scattering process that involving two acoustic phonons and one optical phonon is thought as the fundamental source; this intrinsic scattering process does not occur in materials with a large acoustic-optic frequency gap at high pressure; instead, the scattering between acoustic phonons will dominate.[74] (2) In another case of non-monotonically decreased pressure dependence of κ, *i.e.*, first increase and then decrease with increasing pressure, the competing scattering processes of three-phonon and four-phonon interactions at high pressures,[76] or the interplay between group velocity and phonon relaxation time under pressure,[112] are the possible mechanisms. (3) In the case of diverse pressure dependence of κ revealed in some rare-earth pyrochlores, the competition between the enhancement of group velocity of phonon modes and the reduction of phonon relaxation time determines the pressure dependence.[113]

As pressure can continuously tune materials' lattice dynamics through varying the anharmonicity of atomic/molecular bonding, the interfacial thermal transport behaviors will also be significantly modified. Recent studies show that interfacial stiffness is a crucial parameter for G under pressure, and the interfacial stiffness strongly dominates the thermal transport at weak interfaces but plays a minor role for strong interfaces.[114] Moreover, applying pressure can change the phonon scattering processes across the interfaces, for example, from elastic radiation process to inelastic partial transmission processes through modifying the phonon densities.[79]

3. Characterization methods of thermal-physical properties of materials under pressure

Thermal characterization techniques are normally classified as steady-state and transient methods, for both temperature-dependent and pressure-dependent measurements, and for both bulk and thin-film materials. Within these high-pressure thermal characterization methods, through nearly 100-years development (Figure 1d), the former mainly comprises the thermocouple and heater assisted technique such as Ångström method developed in the Piston-cylinder pressure cell or multi-anvil cell, as well as the thermal grating method, the thermocouple method and Raman-based opto-thermal method applied in DAC, while the later includes the transient hot-wire method for Piston-cylinder pressure cell and pulsed laser transient heating method and time-domain thermoreflectance method for DAC apparatus. Piston-cylinder pressure cell and multi-anvil cell (the normally used is the first-order multi-anvil cell with eight truncated cubic inner anvils) own large size allowing more space for the thermocouple layout, but are normally limited in pressure range below 10 GPa.[33,115-118] However, pressure of at least 20 GPa is usually needed to obtain ~50%

increase in parameters such as the elastic constants that are relevant to thermo-physical properties.[119-123] DAC setup can generate much higher pressure exceeding 100 GPa. However, the very narrow space left between the anvils makes it extremely difficult to spread the wires needed by thermocouples and heaters. Fortunately, recently developed optical contactless methods e.g., Raman opto-thermal method and time-domain thermoreflectance techniques can fulfill the desires to probe the thermal properties at extremely high pressures. These high-pressure thermal characterization methods will be introduced below.

3.1. Steady-state methods

3.1.1. Thermal-couple & heater method in Piston-cylinder pressure cell

The conventional technique to measure the thermal conductivity employs thermocouples and heaters placed together with samples into a symmetric Piston-cylinder pressure cell in the following sequence of *CTSTHTSTC*, where *H* is a heater embedded in the center of the cell, *S* is the sample, *T* is the thermocouple embedded in different regions of the sample for measuring the temperature drop across the sample, and the pressure is applied between two ends of the Piston-cylinder cell (*C*).[33,124,125] The thermal conductivity can be obtained from the temperature gradient measured from the thermal couples embedded across the sample by solving the Fourier's equation of heat conduction (Eq. 2.1). This method has been widely exploited to measure the pressure-dependent thermal conductivity of various polymers up to 0.4 GPa (the limit of Piston-cylinder pressure cell is only a few GPa).[33,124-126]

3.1.2. Ångström method in multi-anvil cell

A thousand-tons press applied in a multi-anvil cell or modern gem anvil cell can push the pressure and temperature limit to ~90 GPa and ~3000 K, respectively, providing a higher pressure and a more convenient steady-state environment for thermal conductivity measurements. Using Ångström method in such a multi-anvil cell, pressure-dependent thermal diffusivities of silica glass and olivine, $CaGeO_3$ perovskite, *etc*., have been successfully measured.[117,118,127] In the Ångström method (see the schematic cross-section in Figure 3a[127]), the sample with a diameter of ~3-4 mm is encapsulated into a cylindrical tube where a graphite- or $LaCeO_3$-like heater is mounted to heat the attached samples up to high temperatures; meanwhile, the thermocouple wires need to be embedded into the sample or fixed next to the sample for temperature measurements. This fabricated sample-containing cylinder is then sealed into a MgO octahedron (with an edge length of ~14-25 mm), and compressed together by 6 outer anvil wedges and 8 tungsten carbide made cubic inner anvils (with ~3-10 mm truncated edge length).[125] Under this apparatus configuration, for instance, using a loading of 900-tons press and inner anvil with truncated length of 3 mm, a

high pressure environment of ~25 GPa can be achieved.[128] Following the above design, applying a sinusoidal temperature wave with a variable frequency in a central wire heater creates a heat wave propagating radially through the surrounding sample of the cylindrical shape. Note that the amplitude and phase of the varying temperature wave are relevant to the thermal diffusivity of the compressed sample. By measuring the amplitude ratio and phase difference of the temperature between the center and outer surface of the sample, the thermal diffusivity at different pressures up to ~20 GPa can be extracted.[115,117,118,129]

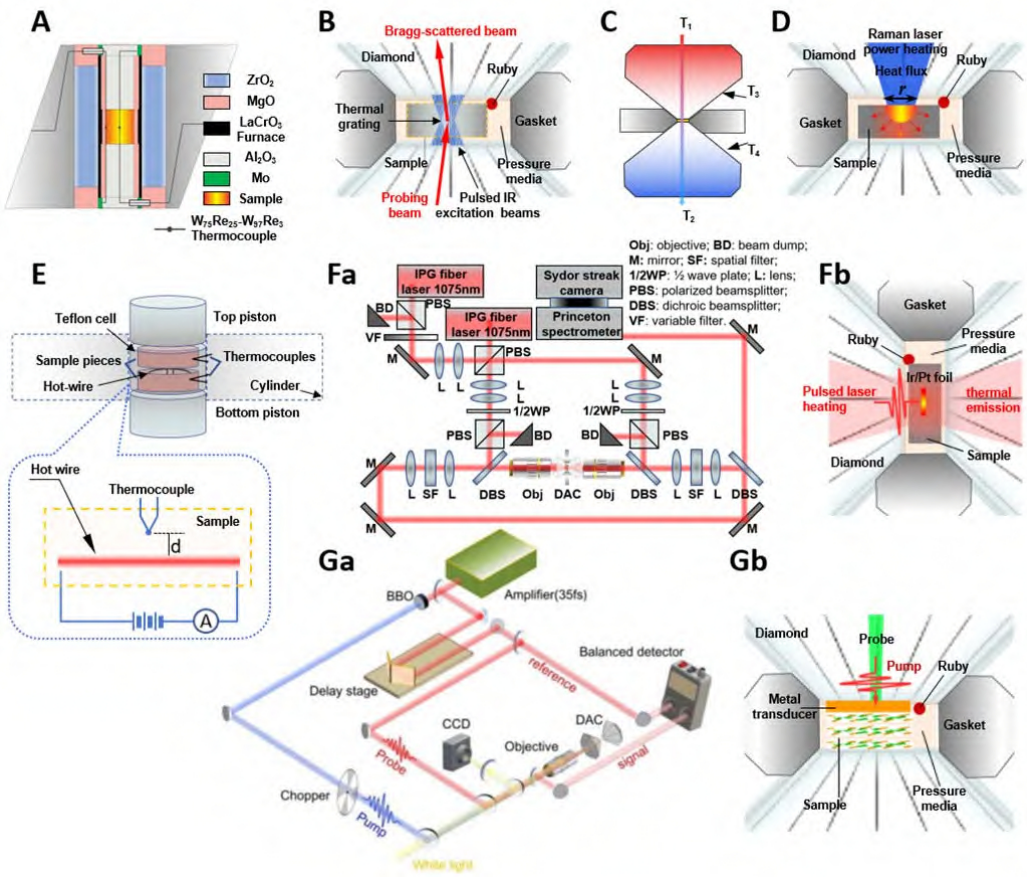

Figure 3 | The schematic of thermal characterization methodologies developed under pressure. A | The Ångström method developed in the multi-anvil cell, **B** | the thermal grating method applied in DAC, **C** | the thermocouple method used in DAC, **D** | the Raman-based opto-thermal method used in DAC, **E** | the transient hot-wire method developed in the Piston-cylinder pressure cell, **Fa-Fb** | the pulsed laser transient heating method applied in DAC, **Ga-Gb** | the time-domain thermoreflectance method and picosecond transient thermoreflectance method applied in DAC. Panels **A-D** are steady-state characterization methods while **E-G** are transient characterization methods. Panels **A-G** are taken or adapted with permission from Refs.[49,109,116,130-135], respectively. ©Elsevier Publishers Limited. ©AIP Publishers Limited. ©Springer Nature Publishers Limited. ©APS Publishers Limited.

3.1.3. Optical thermal grating method in DAC

An optical thermal grating method[131,136,137] compatible with the DAC technique (see Figure 3b) is developed for measuring thermal diffusivity at high pressures up to 12 GPa.[137] In this method, two mode-locked pulse lasers, with the pulses duration of ~80 ps and the laser wavelengths among the sample absorbing range, are incident at an angle of 2θ onto the sample to form a constructive interference with the laser intensity distributed periodically. After absorption, the incident laser produces a periodic distribution of both temperature and refraction index in the sample. Here the period of the thermal grating is defined as $d=\lambda/(2\sin\theta)$, where λ is the laser wavelength. Then a Bragg-diffracting probe pulse is incident onto the same position to monitor the temperature evolution as a function of time. At certain conditions, when the heat diffusion from pulse laser heating can be approximated as one-dimensional, the decay rate of the periodic temperature distribution R_d then can be used to extract the thermal diffusivity of the sample according to $R_d=4\pi^2D/d^2$, where D is the thermal diffusivity. This method is a contactless, optical method which can allow to avoid previous complex and low-efficient fabrication of thermocouple and heater embedded samples.

3.1.4. Thermocouple method in DAC

A thermocouple based steady-state method adapted to the DAC apparatus was recently put forward in 2018 (Figure 3c).[132] Four ultra-tiny thermocouples have been carefully mounted onto the culets/tables parts and the near-culet side-surface parts of diamond anvils, respectively. Then combining a steady-state thermal finite element model (FEM) with the above four-points' temperatures measured from the thermalcouples at each pressure, an actual temperature field distribution within the pressured DAC can be resolved in the FEM based thermal model. Therefore, by adjusting the thermal parameters of the samples until a consistency is achieved between the measured temperature and the model calculated temperature at the exact same positions of the DAC, the thermal conductivity of both diamond anvils and the sample at each pressure and their pressure dependences can be obtained.

3.1.5. Raman-based opto-thermal method in DAC

Phonon frequencies of semiconductors normally display a negative dependence with temperature due to anharmonic effects. Increasing temperature causes the lattice of a material to expand which decreases the frequency of the lattice vibrations (phonons), resulting in a temperature dependent phonon frequency shift; this temperature induced phonon shifts can be directly measured from the Raman spectra thus contactlessly probing the local sample temperature in the laser spot. This principle was later developed into a Raman-based opto-thermal method to measure the thermal conductivity of materials. The principle can be simply described as the

following:

$$\kappa = \left(\frac{2\alpha}{\pi r}\frac{\Delta P}{\Delta T}\right) = \frac{2\alpha}{\pi r}\frac{\chi_{\mathrm{T}}}{\chi_{\mathrm{P}}}, \tag{3.1}$$

where α is the absorption coefficient, ΔP is the incident laser power variation, r is the laser spot radius, ΔT is the temperature variation from spot center induced at the corresponding power variation, while χ_{T} and χ_{P} are the coefficients of temperature dependence and power dependence of Raman mode shifts, respectively.

This method uses the excitation laser from the Raman spectroscopy simultaneously as a local heating source and a thermometer sensor; the Fourier heat transport equation is further solved analytically to extract the thermal conductivity. In detail, first, using an external heat source and conventional thermometry, the temperature dependence of the Raman mode of the sample is measured using low power laser excitation to avoid local heating by laser on the sample; this temperature dependence serves as a calibration which can be used for local temperature determination during the laser heating. This method also requires knowledge of the laser power absorbed in the sample, which can be determined from the absorbance measurements.[109] Then the Raman shift is measured as a function of the laser power, from which the local heating is determined by applying the formerly determined temperature dependence of the Raman frequency. Based on the above principles, a Raman-based opto-thermal method combined with the DAC technique is developed to measure the thermal conductivity of materials at high pressures (Figure 3d). Application of these techniques has made it possible to measure the thermal conductivities of several thermoelectric materials under pressure as well as their pressure dependences.[22,109,138,139]

3.2. Transient methods

3.2.1. Transient hot-wire method in Piston-cylinder pressure cell

The transient technique used to measure the thermal conductivity of materials under pressure generated in a Piston-cylinder pressure cell is the hot-wire method, alternatively termed as Ni-wire assisted electrical-bridge method (see the schematic in Figure 3e). In detail, a Ni-wire was installed into a Piston-cylinder cell together with the target sample and then was electrically heated at a constant power.[116,140-147] At the same time, an electrical-bridge was used to monitor the Ni-wire resistance for recording the temperature change as a function of time. By comparing these data with the temperature evolution as a function of time calculated using a theoretical model, the thermal conductivities of the sample at different pressures can be extracted. Through this method, the room temperature thermal conductivities of CsCl and NaCl at pressures up to 2 GPa, as well as the temperature dependent thermal conductivities of C_{60} and C_{70} at pressures up to 1 GPa were measured.[116,143,148]

3.2.2. Pulsed laser transient heating method in DAC

In 2007, an optical pulsed laser transient heating (TH) method was developed in combination with the DAC techniques to measure the high-pressure high-temperature thermal diffusivity of several minerals at pressures and temperatures as high as 125 GPa and 2600 K.[3,38,60,134,149] In such a TH thermal characterization method (see Figure 3f), a thin metallic coupler (typically, Ir or Pt) needs to be embedded into the target sample; when performing measurements, this metallic coupler is heated by a pulsed laser, resulting in a temperature variation as a function of time generated at its surface; then the surface thermal emission spectrum from the metallic coupler is collected by an all-reflective microscope and analyzed based on the black-body radiation theory. Fitting the measured temperature evolution to the calculated results from a FEM based thermal model, one can extract the thermal diffusivity of the sample at different pressures and temperatures.

More recently, this technique has been modified to enable measurements of metallic samples and to improve the accuracy of determination of thermal conductivity of non-metallic samples. In the modified TH technique,[135] the sample is continuously heated by double-sided lasers to a desired bulk temperature and then a pulsed laser heated from one side generating a heat wave propagating across the sample. The radiative temperatures are then monitored from both sides and the thermal conductivity is further extracted from FEM calculations. It is noted that the TH method is presently one of the limited methods appropriate for high-temperature high-pressure thermal properties measurements, especially for sample temperatures higher than 1400 K. This method has been employed to measure the thermal conductivity of solid Fe at planetary core conditions of ~130 GPa and 3000 K,[3] and later the thermal conductivity of solid Fe and Fe-Si alloys up to 144 GPa and 3300 K[60] and the assemblage of lower mantle minerals crystallized from pyrolite glass at temperatures up to 2500 K at 120 GPa.[150]

3.2.3. Time-domain thermoreflectance method in DAC

Time-domain thermoreflectance (TDTR) is also a contactless optical method that presently being widely applied to measure the thermal conductivity[95,151] and interfacial thermal conductance[105,152] of thin films. The TDTR method can provide a satisfied accuracy of better than 10% and a very fast measurement time; moreover, the technique is readily compatible with DAC operation as the anvils are transparent for visible and near infrared lasers, which are normally used in TDTR. To perform TDTR measurements, a very thin metal film (typically Al, Au, Pt, or Cu with a thickness <100 nm) is usually deposited on one smooth side of the sample, serving as a transducer to absorb thermal energy from the pump laser and transfer the heat to the sample. The fundamental principle of the metal film transducer is that the reflectivity of a material is temperature dependent. For example, for the gold film, the change in its surface reflectivity with temperature is approximately linear to the variations in its

surface temperature within the range of 300-800 K,[153] given by:

$$\frac{\Delta R}{R} = (\frac{1}{R}\frac{\partial R}{\partial T})\Delta T = C_{\mathrm{TR}}\Delta T, \tag{3.2}$$

where C_{TR} is the thermoreflectance coefficient. Notably, the C_{TR} is dependent on the type of metal and the wavelength of the probed reflected light. The thin metal transducer film irradiated by a pulsed pump laser beam and absorbing the laser pulse energy, serves as a periodic heating source. The temperature of the metal transducer film rapidly rises due to the photoexcitation of electrons by the laser pulses. These hot electrons thermalize the optical and acoustic phonons quickly (normally at the picosecond scale). Then the generated heat gradually diffuses into the underlying sample layers at different time scales; this process is governed by the thermal conductivity, heat capacity and density of the materials and by the thermal boundary resistance at the interfaces. The process of heat diffusion in the metal film transducer layer and the sample layers leads to the decay of surface temperature, resulting in the temperature-dependent change of surface reflectivity of the metal film transducer. These reflectivity variations can be monitored by using another pulsed or continuous wave probe laser focused on the same spot as the pump laser. Then, by combining the measured thermoreflectance curve with an analytical or numerical thermal model calculation, the thermal conductivity and interfacial thermal conductance of the sample can be extracted. This method requires that the pump and probe laser spots must be well concentric while the sample surface should be as clean and smooth as possible. The significant advantage of this method is that the sample size can be as small as the laser spot (*i.e.*, ~10 μm diameter), and the characterization temperature can be ranged from liquid nitrogen temperature to few-thousands of Kelvins when depositing the appropriate metal film transducers.

In 2009, the TDTR technique was successfully combined with the DAC technique (*i.e.*, TDTR-DAC technique, see schematic in Figure 3g) to measure the pressure-dependent thermal conductivity of muscovite mica up to 24 GPa.[39] Later, the pressure evolutions of thermal conductivities of various materials from crystals to amorphous polymers were investigated up to 60 GPa using TDTR-DAC technique. To study the effects of variations in thermo-physical parameters of the metal film transducers at high pressures on the extracted thermal conductivities of target samples, the pressure evolutions of critical thermal parameters (*i.e.*, thermoreflectance, piezo-optical coefficient and physical stability) for several metal film transducers (*i.e.*, Ta, Al and Au(Pd) thin films) were further investigated. It was found that the acoustic strengths for Ta and Au(Pd) films are essentially independent of pressure, while it drops abruptly and remains small for the commonly used Al film upon initial loading and up to 12 GPa.[154] Thermal conductivities of liquid pressure transmission mediums under pressure, such as silicone oil and methanol-ethanol mixture, were also measured using TDTR-DAC technique.[155] Furthermore, the ITC (e.g. Al/SiC, Al/graphene/SiO_x/SiC, Al/SiO_x/SiC[114]) as a function of pressure can also be extracted using this method. Based on the TDTR-DAC technique, in 2019, this method was extended to combine with a picosecond pulsed laser based transient thermoreflectance technique to measure the pressure-dependent cross-plane thermal conductivity of

MoS_2 up to 25 GPa.[49,156] Moreover, an *in-situ* method was developed for measuring the high-pressure high-temperature thermal diffusivities of Pt and Fe up to ~60 GPa and 2000 K by combining the thermoreflectance measurements (albeit with ns laser pulses) and laser heated diamond anvil cell techniques.[157]

3.3. Calculation methods

Thermal transport properties of various materials can be theoretically computed as a function of pressure and temperature using a variety of methods including first-principles based phonon Boltzmann transport equation (BTE), density functional theory (DFT) and MD simulations. For example, theoretical calculations of pressure-dependences of lattice thermal conductivities have been performed in iron, argon, diamond, silicon, cubic boron nitride, and so on.[158-163]

A combined DFT and Peierls-Boltzmann transport equation (PBTE-DFT) method was developed and benchmarked against the measured pressure-dependent κ values for a number of materials;[164] in this method, a general quantitative accuracy has been demonstrated without adjustable empirical parameters. The PBTE-DFT method has shown a capability to reliably predict κ of a variety of materials from one-dimensional to bulk under conditions of varying temperature and pressure, including the considerations of defects and higher order anharmonic process. Yet, the PBTE-DFT method has the limitations related to neglecting the effects of temperature oscillating or varying on the material surface with time, and also not accounting for the variations in the phonon distributions near a surface or interface of a material.[164,165] These limitations make PBTE-DFT method questionable in applications (e.g., predicting κ) of materials with extreme disorder or crystals with strong anharmonicity.

MD simulations are another tool for calculating κ; particularly for applications where PBTE-DFT calculations are not effective. To explore the evolution of κ under pressure, an *ab initio* MD was combined with phonon normal mode analysis and the PBTE to predict, for instance, κ of MgO at high temperatures and high pressures.[166] However, only small simulation domains can be handled by *ab initio* MD due to the large computational expense; this makes it most suitable for small nano-structures or bulk materials at high temperatures and high pressures. Another shortage is that the empirical potentials MD simulations needed are often not available for materials of interest. For thermal transport calculations, the potentials need to include essential harmonic and anharmonic phonon properties at the temperatures and pressures of interest, while most empirical potentials were not developed with these characteristics yet.

Recently, a computationally efficient thermal snapshot interatomic force constants (IFCs) fitting technique was developed to obtain the cubic and quartic IFCs that used as important inputs for κ calculations.[76,167,168] In this method, the harmonic forces are subtracted out from the force-displacement dataset using the short and long-range harmonic IFCs within the framework of density functional perturbation theory implemented in the Quantum ESPRESSO, with only the anharmonic IFCs

fitted to the remaining forces. Then both harmonic (second-order) and anharmonic (third and fourth-order) IFCs are used as inputs to determine phonon modes and phonon-phonon scattering rates. The scattering rates are obtained by iteratively solving the PBTE for phonon transport including three-phonon, four-phonon and phonon-isotope scattering terms. The pressure in the calculations was obtained by taking the derivative of the fourth-order anharmonic Helmholtz free energy with respect to volume at each temperature.

4. Thermal properties of materials under pressure

4.1. Gases

Upon compression, gas can undergo gas-liquid-solid transformation. The discussion in this section only refers to the gas naturally existed at ambient conditions. In general, the thermal conductivities of gases under pressure are obviously smaller than those of solids. Figure 4a and Table 1 summarize the κ of several typical gases with respect to pressure. Around 1 GPa, most gases transform into liquids or solids, accompanied by a rapid increase in κ. Limited by experimental techniques, the majority of the thermal studies of gases in the last century was the pressure range within 1 GPa.[77] For instance, κ measurements of hydrogen were carried out using a coaxial cylindrical cell for pressure up to 66 MPa in 1966, and the effects of temperature on κ of hydrogen under pressure were established.[169] Furthermore, pressure-dependent κ parameters of oxygen, methane, nitrogen, neon, argon and other gases, were also investigated mainly via the transient hot-wire method.[170-174] Recently, with the help of DAC and pulsed laser TH techniques, the pressure range of thermal characterizations of gases has been extended over 10 GPa. In 2012, the κ of argon was measured in pulsed laser transiently heated DAC at pressures up to 50 GPa and temperatures up to 2500 K,[175] paving the way for thermal studies of gases at higher pressures. For argon, some theoretical calculations were also performed on predicting its κ at high pressures,[176,177] which provide valuable guidance for experimental studies.

Table 1 | Summary of thermal conductivities for various materials from gases, liquids to solids investigated under pressure.

	Materials	Strain type	Methods	Maximum pressure	Thermal conductivity ($Wm^{-1}K^{-1}$)	Ref.
Gases	Ar	comp.	parallel plate method	240 MPa	0.018-0.107 (1 atm-196 MPa, 298 K)	178
	Ar	comp.	transient hot-wire method	11 MPa	0.018-0.021 (0.58-6.31 MPa, 308 K)	174
	Ar	comp.	transient heating	50 GPa	10.66-78.28 (10-50 GPa,	175

			technique		300 K)	
	Ar	comp.+ tension	MD+BTE calculations	6%comp.+6 %tension	0.1-10 (isotropic strains from -0.06 to 0.06, 20 K)	179
	Ar	comp.	DFT+BTE calculations	150 GPa	3.32-56.71 (10-90 GPa, 400 K)	177
	Ar	comp.	MD calculations	50 GPa	0.72-25.93 (0-50 GPa, 293 K)	176
	N_2	comp.	transient hot-wire method	27.7 MPa	0.038-0.046 (1-27.7 MPa, 470 K)	180
	N_2+CO_2	comp.	transient hot-wire method	30 MPa	change with proportion	180
	H_2	comp.	transient short hot-wire method.	99 MPa	0.197-0.28 (0.26-97.76 MPa, 323 K)	181
	H_2	comp.	-	66 MPa	0.19-0.24 (3.54-65.6 MPa, 298 K)	169
	Ne	comp.	parallel plate method	260 MPa	0.05-0.12 (1 atm-250 MPa, 298 K)	173
	Methane	comp.	transient hot-wire method	70 MPa	0.0337-0.1169 (0.99-67.3 MPa, 295 K)	171
	O_2	comp.	transient hot-wire method	70 MPa	0.028-0.068 (2-65.3 MPa, 310 K)	170
Liquids	Toluene	comp.	ac-heated wire method	1000 MPa	0.128-0.25 (0-902.6 MPa, 300 K)	182
	H_2O	comp.	line heat source probe	700 MPa	0.65-0.82 (108-700 MPa, 298 K)	183
	H_2O	comp.	TDTR+DAC	22 GPa	0.54-24.69 (0-22 GPa, 300 K)	184
	H_2O	comp.	transient hot-wire method	0.8 GPa	0.56-1.54 (0-0.65 GPa, 273-243 K)	185
	Silicone oil	comp.	TDTR+DAC	23 GPa	0.16-1.53 (0-23 GPa, 300 K)	155
	4:1 Methanol-ethanol	comp.	TDTR+DAC	23 GPa	0.21-1.98 (0-23 GPa, 300 K)	155
Earth materials	Muscovite	comp.	TDTR+DAC	24 GPa	0.46-6.6 (0-24 GPa, 300 K)	39
	(Mg, Fe)O (Mg, Fe)SiO_3	comp.	TH+DAC	133 GPa	-	134
	(Mg, Fe)O	comp.	TDTR+DAC	120 GPa	2.8-50 (0-120 GPa, 300 K)	186
	(Mg, Fe)SiO_3	comp.	TDTR+DAC	120 GPa	5-30 (0-120 GPa, 300 K)	187
	(Mg, Fe)CO_3	comp.	TDTR+DAC	67 GPa	2.5-45 (0-67 GPa, 300 K)	188

	MgO	comp.	TDTR+DAC	60 GPa	53-161 (0-60 GPa, 300 K)	189
	MgO	comp.	DFT+P-BTE calculations	150 GPa	66-341 (0-150 GPa, 300 K) 2-46 (0-150 GPa, 3000 K)	190
	$MgSiO_3$	comp.	TDTR (two-side) +DAC	144 GPa	8-37.1 (11-144 GPa, 300 K)	191
	Pyrolite	comp.	TH+DAC	124 GPa	3.9 (0-80 GPa, 2000-2500 K) 5.9 (0-124 GPa, 2000-3000 K）	150
	Ringwoodite	comp.	TDTR+DAC	25 GPa	3-16 (0-25 GPa, 300 K)	192
	δ -(Al,Fe)OOH	comp.	TDTR+DAC	110 GPa	5-60 (0-110 GPa, 300 K)	193
	Iron	comp.	TH+DAC	130 GPa	20-40 (35-130 GPa, 2000-3000 K)	3
	Iron	comp.	TDTR+DAC	120 GPa	76-120 (0-120 GPa, 300 K)	60
	$Fe_{0.96}Si_{0.04}$	comp.	TDTR+DAC	125 GPa	16.5-60 (0-125 GPa, 300-3300 K)	60
	$Fe_{0.85}Si_{0.15}$	comp.	TDTR+DAC	144 GPa	11.5-40 (0-144 GPa, 300-3300 K)	60
	hcp Iron	comp.	TH+DAC	134 GPa	70-80 (constant above 46 GPa)	111
	Iron	comp.	DFT calculations	340 GPa	150-250 (120-340 GPa, 4500-6500 K)	2
Thermoelectric materials	$Pb_{0.99}Cr_{0.01}Se$	comp.	opto-thermal Raman	6 GPa	2.1-8.2 (0-6 GPa, 300 K)	22
	PdS	comp.	opto-thermal Raman	10 GPa	25-9 (0-10 GPa, 300 K)	139
	$CuInTe_2$	comp.	opto-thermal Raman	8 GPa	2.1-8.2 (0-8 GPa, 300 K)	109
	$CuInTe_2$	comp.	BTE calculations	5 GPa	7.5-4.1 (0-5 GPa, 300 K)	194
Electronic materials	MoS_2	comp.	ps-TTR+DAC	19 GPa	3.5-25 (0-19 GPa, 300 K)	49
	Si	comp.	TDTR+DAC	45 GPa	73-300 (0-36 GPa)	195
	$Si_{0.991}Ge_{0.009}$	comp.	TDTR+DAC	45 GPa	24-360 (0-36 GPa)	195
	Si	torsion	TDTR+DAC	24 GPa	142-7.6 (0-24 GPa, 300 K)	196
	Si	comp.+ tension	MD+BTE calculations	3%comp.+3 %tension	135-155 (isotropic strains from -0.03 to 0.03, 300 K)	179
	Si	comp.+ tension	MD calculations	4%comp.+4 %tension	100-450 (Stillinger and Weber Si potentials, 300 K)	197
	Monolayer silicene	comp.	DFT+BTE calculations	10%	25-170 (0-10% strain, 300 K)	198
	Monolayer h-BAs	tension	MD calculations	3-7%	180.2-375 (3% strain along armchair direction)	199

				180.2-406.2 (3% strain along zigzag direction)	
	BAs	comp.	DFT+BTE calculations	80 GPa	1331-823 (0-80 GPa, 300 K）	76
	GaAs	comp.	DFT+BTE calculations	20 GPa	49-70 (0-16 GPa, 300 K)	108

* "-" in the table means that the original papers did not mention the item. The acronyms "comp.", "MD", "BTE", "DFT", "TH", "TDTR", "TTR", and "DAC" represent "compression", "molecular dynamics, "Boltzmann transport equation", "density-functional theory", "pulsed laser transient heating", "time-domain thermoreflectance", "transient thermoreflectance", and "diamond anvil cell", respectively.

4.2. Liquids

Most studies on the κ parameters of liquids under pressure, on the one hand, were previously focused on organic liquids such as oil, ethanol, toluene to explore their implications on food and industrial products.[182,183,200] On the other hand, interests on the pressure-dependent κ of pressure transmitting medium used in DAC were attracted,[155] such as the methanol-ethanol mixture and silicone oil, which can provide the fundamental parameters for the accurate study of thermal conductivity or interfacial thermal conductance of other materials under pressure. In addition, H_2O, as one of the most important substances in life, was also systematically studied on its κ under pressure.[184,201] The evolution of the κ of the above-mentioned liquids as a function of pressure is plotted in Figure 4b and summarized in Table 1, showing typical changes of the orders of 0.1 to 10 $Wm^{-1}K^{-1}$ within the transformation range from liquids to solids.

4.3. Solids

Pressure dependence of the thermal transport in solids and amorphous materials has been studied for approximately 40 years. Here, we discuss the progress in pressure dependent thermal conductivities of Earth materials, thermoelectric materials, two-dimensional layered materials, semiconducting electronic materials, and the interfacial thermal conductance at solid-solid interfaces (Figure 4-6 and Table 1).

4.3.1. Earth materials

Understanding the heat transport and thermal evolution of Earth's interior requires knowledge of κ of minerals and melts at relevant extreme temperatures and pressures. In Earth's core, the thermal evolution and the energies driving the geomagnetic field are highly sensitive to the κ of core materials at high pressure and high temperature conditions, because these κ values will define the adiabatic heat flux, thermal and compositional energy that are available to support the operation of Earth's magnetic field. Meanwhile, κ of the Earth's lower mantle minerals greatly

impacts the mantle convection style and affects the heat conduction from the core to the mantle. Note that conduction is the major heat transfer mechanism at the core-mantle boundary, in which κ value of the bottom boundary layer of the mantle determines the magnitude of heat flux from the core. More importantly, this κ value is intimately related to the instability of the boundary layer, the formation of mantle plumes, the long-term thermal evolution of both mantle and core, and the driving force for the generation of the geomagnetic field.

Earth's core is composed of iron (Fe) alloyed with some light elements. A wide range of κ of Fe and its alloys have been theoretically predicted at core conditions. Experimentally, the κ of solid Fe which is about 18-44 $Wm^{-1}K^{-1}$ at pressures (130 GPa) and temperatures (3000 K) of the core condition was directly measured, using a dynamically double-sided infrared continuous-wave lasers heated DAC with one-side additional thermal disturbance created by another infrared pulsed laser.[3,135,202] Recently, an increased κ of γ-Fe (90-125 $Wm^{-1}K^{-1}$) and in a mixed phase of Fe (45-65 $Wm^{-1}K^{-1}$) with increasing pressure up to about 46 GPa was measured, through a single-sided laser heated DAC technique where the power absorbed by a Fe metal foil at hotspot was calculated from a thermodynamic simulation in the COMSOL software.[111] While κ of ε-Fe lies in the range of 70-80 $Wm^{-1}K^{-1}$ at 1600-2100 K (with an error of ~40%) and is almost independent of pressure up to 134 GPa; this independent κ of ε-Fe was attributed to the strong electronic correlation effects driven by the electronic topological transition.[111] In addition, the high pressure κ of solid Fe and Fe-Si alloys was measured at both room temperature and high temperature up to 144 GPa and 3300 K by the combination of TDTR[39] and TH method.[3,38] It was found that at room temperature, κ of solid Fe increases from ~76 $Wm^{-1}K^{-1}$ to ~90 $Wm^{-1}K^{-1}$ at ~13 GPa and then decreases to a minimum of ~40 $Wm^{-1}K^{-1}$ at around 40 GPa, followed by a further increase again reaching ~130 $Wm^{-1}K^{-1}$ when the pressure is near the core-mantle boundary (CMB) condition (120 GPa); this minimum may be due to an electronic topological transition occurring at ~40 GPa. Addition of Si impurity significantly lowers κ of pure Fe, for example, 16.5 $Wm^{-1}K^{-1}$ for $Fe_{0.96}Si_{0.04}$ and 11.5 $Wm^{-1}K^{-1}$ for $Fe_{0.85}Si_{0.15}$, respectively, at ambient conditions. With increasing pressure, thermal conductivities of both $Fe_{0.96}Si_{0.04}$ and $Fe_{0.85}Si_{0.15}$ increase monotonically up to 40 GPa, and then saturate at ~40 $Wm^{-1}K^{-1}$ and 19 $Wm^{-1}K^{-1}$, respectively (Figure 4c). However, at high temperature of ~3300 K, κ of $Fe_{0.85}Si_{0.15}$ firstly increases to ~40 $Wm^{-1}K^{-1}$ (80 GPa) and then decreases to ~20 $Wm^{-1}K^{-1}$ (144 GPa), while κ of $Fe_{0.96}Si_{0.04}$ increases to ~60 $Wm^{-1}K^{-1}$ (125 GPa, Figure 4d).[60] All of these κ values measured by experimental methods are several times lower than those obtained by calculation and electrical resistivity measurements.[2,4,203-205]

In the earlier recognition, MgO is thought as a typical mineral of lower mantle materials. The κ of MgO has been calculated through a numerical technique combined with the PBTE-DFT method, providing a model for the P-T dependence of the κ of MgO at conditions from ambient to the CMB.[190,206] It was found that κ increases from 15-20 $Wm^{-1}K^{-1}$ at the pressure of the 670 km seismic discontinuity to 40-50 $Wm^{-1}K^{-1}$ at the CMB pressure. Furthermore, it was found that at 2000 K, κ of MgO measured via the TH technique has about 50% enhancement when pressure increases

from ambient to 32 GPa; it was also revealed that the radiative part of κ of the lower mantle increases with depth until saturate to ~0.54 $Wm^{-1}K^{-1}$ at the depth of CMB.[38,134,207-210] However, at 300 K, through TDTR measurements in DAC, κ of MgO was found increasing from 50 $Wm^{-1}K^{-1}$ at ambient conditions to about 160 $Wm^{-1}K^{-1}$ at 60 GPa, agreeing well with the previous model and first-principles predictions.[190,211,212] Concerning other Earth minerals, recent investigations on the pressure dependences of κ of other lower mantle minerals include (Mg,Fe)O,[186] (Fe,Mg)SiO_3,[187] $(Fe_{0.78}Mg_{0.22})CO_3$,[188] δ-(Al,Fe)OOH,[193] $Mg_{0.94}Fe_{0.06}SiO_3$,[213] $(Mg_{0.9}Fe_{0.1})O$,[213] $Mg(OH)_2$,[214] $CaGeO_3$,[127] $(Mg_{0.9}Fe_{0.1})_2SiO_4$,[14] olivine $(Mg_{0.9}Fe_{0.1})_2SiO_4(Fo_{90})$,[215] ringwoodite,[192] *etc*. Among them, thermal anomalies were found in an important water-carrying mineral δ-(Al,Fe)OOH, of which the κ varies drastically by 2-3 fold when compressed across the spin transition of iron, thus leading to an abnormally low κ value at the lowermost mantle pressure.[193] Similar anomalous pressure dependence of κ was also observed in the mineral of $(Fe_{0.78}Mg_{0.22})CO_3$ when pressurized across the spin transition zone.[188]

As an important mineral in Earth's lower mantle near the CMB, the κ of $MgSiO_3$ was found to be about 11 $Wm^{-1}K^{-1}$ at 144 GPa, increasing nearly 6 times than that at ambient condition, when measured by a modified TDTR technique in which the pump and probe lasers illuminate the opposite sides of the sample of the DAC.[191] Through non-equilibrium MD simulations, the κ values of $MgSiO_3$ at 1000 K show enhancements from 8.5 $Wm^{-1}K^{-1}$ to 14-20 $Wm^{-1}K^{-1}$ in the range of 20-130 GPa with an obvious anisotropy. Note that these recently measured and calculated values are within the range of previous estimates of κ values at the CMB (4-29 $Wm^{-1}K^{-1}$).[216-218,150,186,187,191,219-224]

4.3.2. Thermoelectric materials

Thermoelectric (TE) materials with a high-efficient figure-of-merit (*zT*, which is normally expressed as $zT=\sigma S^2T/\kappa$, where S is the Seebeck coefficient) are an ideal candidate to overcome the future energy crisis by transforming waste heat into power generation. The current bottleneck is that the *zT* is still too low to achieve a value of >3 for practical applications, according to the present modulation methods such as doping, alloying, temperature, and nanostructure engineering. Pressure as a fundamental thermodynamic variable can modify physical (such as crystal structure, electrical and magnetic) properties and chemical properties even at room temperature through the lattice compression, thus enables pressure-tuning as a promising and reliable approach to modulate the thermoelectric properties, including electrical conductivity and thermal conductivity, ultimately achieving high *zT* values.

Through the aforementioned DAC combined Raman opto-thermal method, the pressure dependence of κ was measured in a strained TE material of $CuInTe_2$,[109] and it is found that the κ significantly reduces from 11.7 $Wm^{-1}K^{-1}$ to a minimum of 4.1 $Wm^{-1}K^{-1}$ at 2.2 GPa. When the pressure increases to above 6 GPa, where the material undergoes a transition into a new phase, the κ jumps to ~30 $Wm^{-1}K^{-1}$ and keeps increasing to about 40 $Wm^{-1}K^{-1}$ until 7.9 GPa where all the Raman modes almost

vanish (Figure 4e). Pressure-induced phonon anharmonicity and phonon softening are thought as the main mechanism for such a reduction of κ under pressure. It is interesting that the κ of another TE material PbS continuously decreases from about 25 $Wm^{-1}K^{-1}$ at ambient to about 9 $Wm^{-1}K^{-1}$ at near 4 GPa and then saturates until about 11 GPa.[139] A continuous decrease of κ is also witnessed in a half-Heusler TE material FeNbSb, which decreases from ~5 $Wm^{-1}K^{-1}$ at ambient to ~2 $Wm^{-1}K^{-1}$ at the pressure of 18 GPa.[138] Recently, a significantly enhanced room temperature *zT* value of ~1.7 (~4 times enhancement) was reported at about 2.8 GPa in a Cr-doped PbSe within the DAC, and this enhancement was ascribed to a pressure driven topological phase transition at 2.6 GPa.[22] In this work, via a similar Raman opto-thermal method, an increase of κ from ~2 $Wm^{-1}K^{-1}$ at ambient condition to ~6 $Wm^{-1}K^{-1}$ at 4.8 GPa was observed, followed by an immediate jump to a larger value of ~8 $Wm^{-1}K^{-1}$ due to the transition into a *Pnma* phase (Figure 4e).

Many new results have been also achieved through first-principles calculations, for instance, the strain engineering effect on the κ of the commercial low-temperature TE material Bi_2Te_3 was simulated with a 50% reduction shown in κ when under a 6% tensile strain, while a 61% increment when under a 4% compressive strain.[225] Via similar calculation methods, the κ of skutterudites $CoSb_3$ and $IrSb_3$ (medium-temperature TE materials) both exhibit an approximate parabolic trend with respect to pressure at the same temperature.[226] $CoSb_3$ has an increased κ from ~11.3 $Wm^{-1}K^{-1}$ at ambient condition to ~13.3 $Wm^{-1}K^{-1}$ at the maximum *zT* value's (*zT*=1.09) pressure of 58 GPa, despite the largest κ of ~18.6 $Wm^{-1}K^{-1}$ appearing at ~30 GPa. Meanwhile, $IrSb_3$ shows a decreased κ from ~14.2 $Wm^{-1}K^{-1}$ at ambient condition to ~8.8 $Wm^{-1}K^{-1}$ at its maximum *zT* value's (*zT*=1.4) pressure of 54 GPa, with its largest value of ~25.4 $Wm^{-1}K^{-1}$ turning up at ~20 GPa.

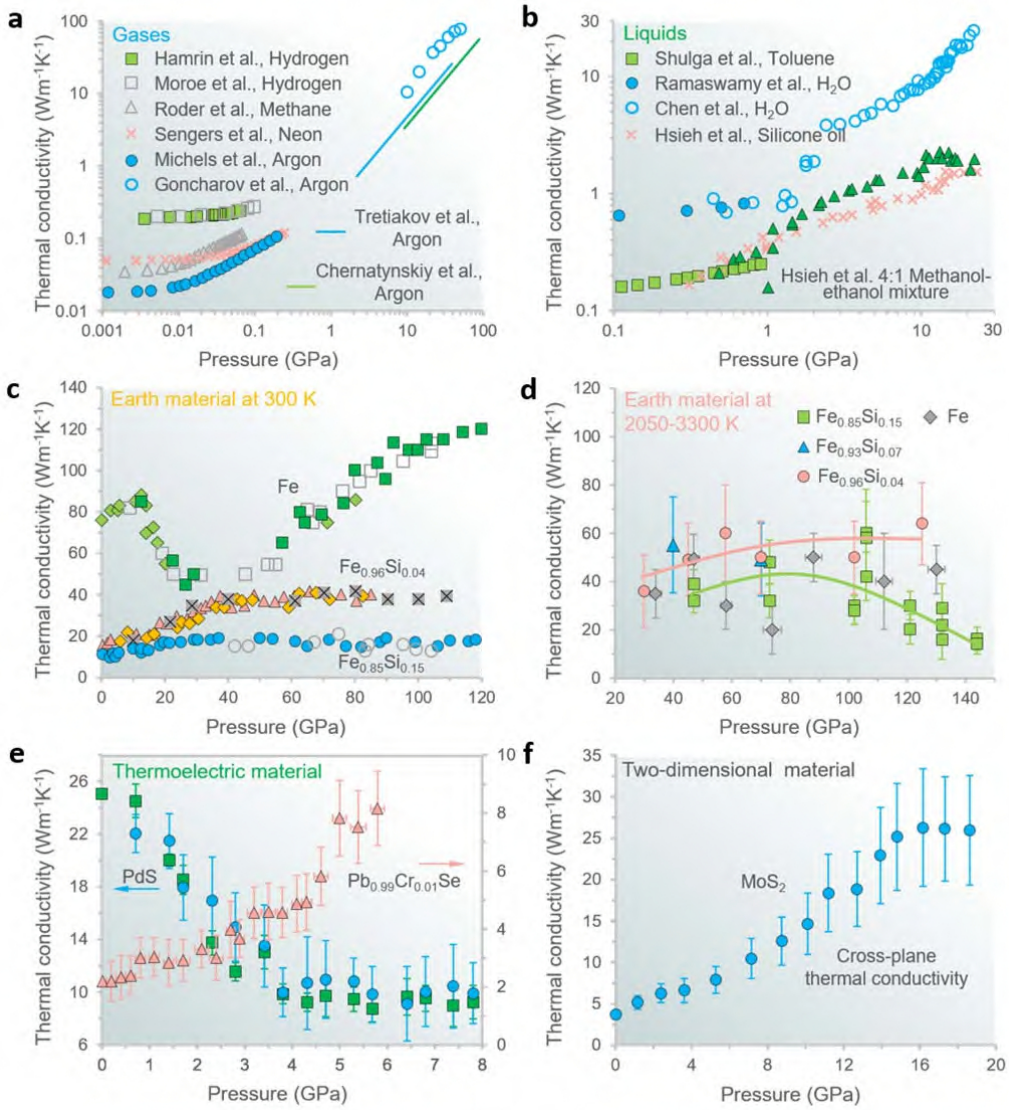

Figure 4 | Thermal conductivities of gases, liquids, Earth, thermoelectric and two-dimensional materials under pressure. a | Pressure dependence of the thermal conductivity of hydrogen, neon, argon, and methane gases. The values are taken from Refs. [169,171,173,175-178,181]. **b** | Pressure dependence of the thermal conductivity for liquids of H_2O, silicone oil, methanol-ethanol mixture, and toluene. The values are taken from Refs[155,182-184]. **c** | Thermal conductivities of Earth materials as a function of pressure for iron and iron-silicon alloys up to 120 GPa at 300 K. **d** | Thermal conductivities of Earth materials as a function of pressure for iron and iron-silicon alloys up to 144 GPa and 3300 K. The values are taken from Refs.[3,60]. **e** | Thermal conductivities of thermoelectric materials with respect to pressure for $Pb_{0.99}Cr_{0.01}Se$ and PbS at 300K. The values are taken from Ref.[22,139]. **f** | Pressure dependence of the thermal conductivity for two-dimensional material MoS_2. The values are taken from Ref.[49]. Lines in panels **a** and **d** are simulation results. Panels **c-f** are adapted with permission from Refs.[3,22,49,60,139]. ©Springer Nature Publishers Limited, ©APS Publishers Limited. ©Elsevier Publishers Limited.

4.3.3. Two-dimensional layered materials

Extreme strain has a very sensitive and profound impact on phonon transport properties that are correlated to the κ modulation of two-dimensional layered materials. These materials normally possess highly anisotropic thermal conductivities along the in-plane and cross-plane directions due to their weak interlayer bonding by van der Waals force. For example, the reported in-plane thermal conductivity ($\kappa_{//}$, ranging from 35-85 $Wm^{-1}K^{-1}$ at ambient condition) of MoS_2,[227-229] an archetypal transition-metal-dichalcogenide (TMDs) with a layered crystal structure, is more than 10 times larger than the cross-plane thermal conductivity ($\kappa_{\perp}$, about 2–4.5 $Wm^{-1}K^{-1}$).[227,230,231] Small $\kappa_{\perp}$ could jeopardize heat dissipation of TMDs-based electronics, while strain engineering or high pressure techniques are promising to enhance and modulate the $\kappa_{\perp}$, which can also revolutionize the tunability and thermal management engineering techniques in all TMDs-based electronic devices. Despite extensive theoretical studies of strain's effect on κ in TMDs, no consistent conclusions have been drawn.[72,78,232,233] The pressure dependence of κ of bulk MoS_2 up to 25 GPa was experimentally obtained for the first time in 2019.[49] An increase of $\kappa_{\perp}$ from 3.5 $Wm^{-1}K^{-1}$ at ambient condition to about 25 $Wm^{-1}K^{-1}$ at ~25 GPa was observed using a picosecond transient thermoreflectance technique, as shown in Figure 4f. Combined with coherent phonon spectroscopy and first-principles calculations, it was further revealed that the drastic change in $\kappa_{\perp}$ arises from the strain enhanced interlayer interaction, heavily modifying the phonon dispersion curves, and decreasing the phonon lifetime. In general, this enhancement in $\kappa_{\perp}$ is mainly attributed to the unbundling effect along the cross-plane direction, while the change of electronic thermal conductivity under pressure has negligible contribution. The strain effects on many other two-dimensional materials are still experimentally unexplored.

An abnormal strain-dependence is recently shown in a novel hexagonal phase monolayer BAs. Through DFT+BTE calculations, the $\kappa_{//}$ was predicted to be enhanced to 375.0 $Wm^{-1}K^{-1}$ and 406.2 $Wm^{-1}K^{-1}$ from 180.2 $Wm^{-1}K^{-1}$ along the armchair and zigzag directions, respectively, under only 3% stretching.[199] This enhancement is correlated to the fact that stretching makes the flexural out-of-plane mode being the dominant heat carrier.

4.3.4. Semiconductor electronic materials

High κ of semiconducting electronic materials is the key for efficient device thermal dissipation and thermal management. Many methods have been tried to improve their κ values, however applications of pressure remains underexplored even though the available in the literature data suggest enhanced materials thermal performance. Up to date, the majority of works on the pressure dependence of κ in semiconducting electronic materials are performed by first-principles calculations. By means of separate calculations of the harmonic and anharmonic effects of strain on

materials stiffness and phonon properties, the κ of the widely used Si semiconductor is found constant within a 3% compression (equivalent to ~4 GPa) and only has about 10% decrease when it is under a 3% tension; this was mainly ascribed to the anomalous behavior of its phonon lifetime which increases with the strain when moving from compression to tension and allows greater root-mean-square displacement under compression. Experimentally, the κ of Si as a function of pressure up to 45 GPa was measured via TDTR (see Figure 5a). In contrast to the above predictions, a κ of 115-130 $Wm^{-1}K^{-1}$ within the entire diamond cubic phase range of 0-13 GPa was observed in Si without obvious pressure dependence, while a continuously increased κ to ~300 $Wm^{-1}K^{-1}$ was witnessed within the metallic phase in the range of 16-36 GPa.[195] Meanwhile, the pressure dependence of κ of $Si_{0.991}Ge_{0.009}$ was also measured revealing an increasing trend in both pressure regions of the semiconducting phase and the metallic phase, but accompanied with a jump between the diamond cubic phase and the primitive hexagonal phase at ~13 GPa as well as a sharp drop between the primitive hexagonal phase and the intermediate *Cmca*/*hcp* phase at ~36 GPa.[195] Moreover, via the combined density functional perturbation theory with the phonon Boltzmann equation, a dramatically increased κ of ~12000 $Wm^{-1}K^{-1}$ for the ultra-wide bandgap natural diamond (~17000 $Wm^{-1}K^{-1}$ for isotope-pure diamond, Figure 5b) at room temperature and 400 GPa was predicted; the overall increased frequency scale with pressure that results in the higher acoustic velocities and lower phonon-phonon scattering rates is regarded as the primary mechanism for this enhancement, *i.e.*, an increase in the optical mode frequencies with pressure weakens the acoustic-optical coupling thus driving the κ of diamond to far higher values (Figure 5b).[234]

Interestingly, many anomalous pressure dependences of κ were reported in some binary compound semiconductor materials especially those of large mass ratio. For example, the pressure dependences of κ of several binary compounds with a set of widely varying mass ratio are examined using a first-principles approach, *i.e.*, GaAs, SiC, BN, BP, BSb, BAs, BeTe and BeSe.[74] The calculations revealed that those compounds with similar mass ratio, such as GaAs, SiC, BN and BP, show an increased κ with pressure, while compounds with large mass ratio (e.g., BSb, BAs, BeTe, BeSe) that have significant frequency gaps between the acoustic and optic phonons exhibit a decreasing κ with pressure (Figure 5c). These anomalously decreased pressure dependence were found arising from the fundamentally different nature of the intrinsic scattering processes for heat-carrying acoustic phonons, *i.e.*, the common three-phonon scattering process that involve two acoustic phonons and one optical phonon does not occur due to the large acoustic-optical frequency gap; instead, the scattering between acoustic phonons dominate at high pressures thus limiting κ. Some more interesting calculations were recently reported on BAs, for example, a different non-monotonic pressure dependence of κ was calculated and shown to firstly increase as most material and then decrease at high temperatures. This was further revealed due to the competing responses of three-phonon and four-phonon interactions to pressure.[76] Based on the first-principles calculations combined with phonon Boltzmann transport equation,[113] the κ of wide-bandgap bulk GaN in the

normal-pressure range of wurtzite phase and high-pressure rocksalt phase (Figure 5d) was calculated, showing that at the wurtzite-to-rocksalt phase-transition pressure, the κ of GaN has a sharp reduction of 91%, then increases almost linearly within the rocksalt phase range until 68 GPa; in addition, the κ of wurtzite GaN exhibites a nonmonotonic dependence on pressure with an ~66% increase first up to ~20 GPa then a slow decrease until the phase transition pressure.[112] According to phonon mode analysis, the sharply reduced κ of the rocksalt phase was ascribed to the enhanced lattice anharmonicity, while the nonmonotonic pressure-dependence of κ in wurtzite GaN was attributed to the interplay between group velocity and phonon relaxation time.[112]

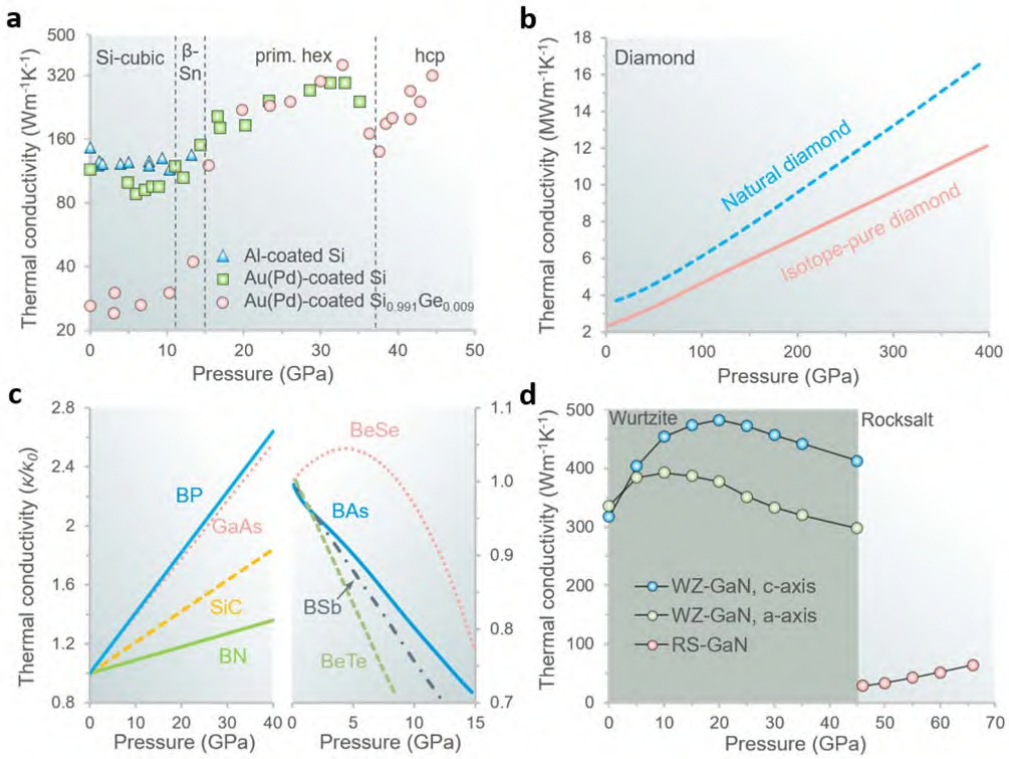

Figure 5 | Thermal conductivities of semiconducting electronic materials under pressure. The thermal conductivity as a function of pressure for **a** | electronic materials of Si and $Si_{0.991}Ge_{0.009}$ measured using TDTR near room temperature within the range of 0-45 GPa. The predicted pressure dependence of the thermal conductivity from first-principles calculations for **b** | the natural and isotope-purified ultra-wide bandgap diamond at 300 K up to 400 GPa, **c** | binary compound semiconductors of GaAs, SiC, BP and BN with an increasing trend, and BAs, BeTe and BSb with a decreasing trend, and BeSe with a non-monotonic trend. **d** | Predicted nonmonotonic pressure dependence of the thermal conductivity for wide bandgap semiconductors of GaN across their phase transition pressures. Panels **a-d** are adapted with permission from Refs.[74,112,195,234], respectively. ©APS Publishers Limited.

968 **4.3.5. Solid-solid interfaces**

969 When heat transfers across an interface, an unavoidable temperature drop exists
970 at the interface, making the original interfacial thermal conductance *G* (or inversely,
971 thermal boundary resistance, TBR) critical in controlling heat conduction through
972 interfaces, especially for the cases of solid-solid interfaces that are widely involved in
973 nanostructures, nanoscale composites, and superlattices.[64,235-239] For instance, the
974 effective thermal conductivity of materials can be reduced to be lower than that of the
975 amorphous limit by introducing a high density of interfaces through nanostructure
976 engineering; in this way, the thermoelectric energy conversion can be improved.[95,151]
977 According to the present theoretical understanding, the more dissimilar the densities
978 of phonon vibrational states of the two materials of the interface, the lower the *G*;
979 however, a variety of anomalous interfacial thermal transport behaviors contradicting
980 the theoretical predictions were experimentally observed especially in examples of
981 metal/diamond interfaces.[102] The effect of interfacial bonding on interfacial thermal
982 transport has been extensively discussed. Lattice-dynamic theory illustrates that weak
983 interfacial bonding can significantly lower *G*.[240] The MD simulations also showed
984 that the low interfacial stiffness can suppress *G*.[241,242] In the case of extremely weak
985 interfacial bonding, *G* scales with the square of the interfacial force constant, while in
986 the strong interfacial stiffness condition, *G* saturates at the AMM predicted value.
987 The interfacial stiffness can be modulated by an applied stress through a
988 generated discontinuity in displacement. The applied pressure can enable continuous
989 tuning of materials lattice dynamics through varying the anharmonicity of atomic or
990 molecular bonds,[77] and allow the direct observation of the role of the interfacial
991 bonding on the suppression of *G* (Figure 6a-d). For example, on the ITC comparison
992 of three types of interfaces loaded in DAC with the interfacial bonding from strong to
993 weak, *i.e.*, the pressure dependent *G* values of clean Al/SiC, Al/SiO_x/SiC and
994 Al/graphene/SiO_x/SiC interfaces measured by the TDTR method, it was found that *G*
995 of the strong Al/SiC interface (~200 MW/m^2K) weakly depends on the pressure,
996 while *G* of the weak Al/SiO_x/SiC and Al/graphene/SiO_x/SiC interfaces (~30 MW/m^2K
997 at ambient, Figure 6c) increases rapidly with pressure and approaches the similar
998 value of the strong Al/SiC interface at >8 GPa. These results demonstrate that the
999 interfacial stiffness dominates the thermal transport at weak interfaces but plays a
1000 minor role for strong interfaces.[114] The alloying of semiconductors will also affect the
1001 behaviors of *G* at their interfaces, for instance, on the examples of the
1002 pressure-dependent *G* between the Al and Au(Pd) transducers and the Si and Si(Ge)
1003 substrates measured by the regular and beam-offset TDTR up to 45 GPa, a nearly 50%
1004 enhanced *G* was observed at the Al/Si interface with a 2.2 nm native oxide layer
1005 which increases from 260 to 380 MW/m^2K between 0 and 10 GPa.[195] It was also
1006 found that the difference in the initial *G* between Au(Pd)/Si and Au(Pd)/Si(Ge) due to
1007 the different interfacial bonding is suppressed at 10 GPa. After crossing the
1008 semiconductor-metal phase transition at ~15 GPa, *G* of Au(Pd)/Si and Au(Pd)/Si(Ge)
1009 increases to a discontinued higher average values of 750 and 470 MW/m^2K with weak
1010 pressure dependence, respectively (Figure 6d).[195] For much strongly bonded

interfaces, G of Al/MgO interface increasing from ~0.5 to 1.1 GW/m^{2}K and G of $SrRuO_3/SrTiO_3$ interface increasing to ~0.8 GW/m^{2}K within the 0-60 GPa range were observed using a similar experimental method(Figure 6b).[243] All these comparisons under pressure indicate that interfacial stiffness is an influential parameter for G, even when the interface is relatively clean and strongly bonded.

Many metal-diamond interfaces show a G anomalously higher (such as Au and Pb, 5-10 times) than those values predicted by the elastic phonon radiation limit model;[102,105] this means significant inelastic phonon scattering processes are probably involved. To enable the study of inelastic processes and understand the hidden mechanism, it would be beneficial to investigate an extreme situation of weakly bonded metal-diamond interfaces. Also, applying high pressure can extend the metal phonon density of states to significant higher frequencies and stiffen the interfacial bonding greatly to suppress the extrinsic effects. By applying pressure in a DAC up to 50 GPa via TDTR to measure G of metal-diamond interfaces for Pb, Au(Pd), Pt and Al films deposited on diamond anvils, it was observed that in all cases G increases weakly or saturates to similar values at high pressures (Figure 6a-b).[79] To understand this tendency, it was proposed that the anharmonic conductance at metal-diamond interfaces is controlled by partial transmission processes, which means that a diamond phonon inelastically scatters at the interface and absorbs or emits a metal phonon.[79]

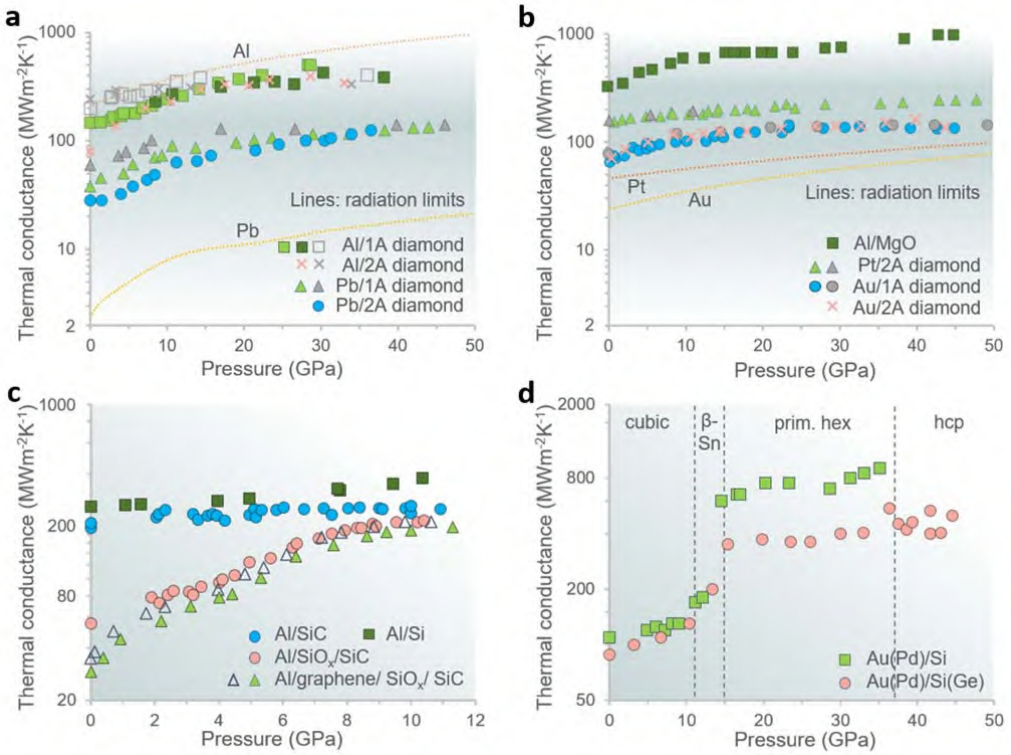

Figure 6 | Pressure dependence of the interfacial thermal conductance at solid-solid interfaces. A various range of interfacial thermal conductance with different interfacial stiffness at solid-solid interfaces were measured under pressure at examples of diamond based **a** | Al/diamond and Pb/diamond interfaces, and **b** | Au/diamond and Pt/diamond interfaces up to 50 GPa (lines are

predictions by the elastic phonon radiation limit model), as well as at examples of Al film transducer based strongly bonded Al/MgO interfaces up to 45 GPa, and **c** | strongly bonded Al/Si and Al/SiC interfaces, and weakly bonded Al/SiO_x and Al/graphene interfaces up to 12 GPa. The interfacial thermal conductance measured under pressure at examples of Au(Pd) film transducer based **d** | weakly bonded Au(Pd)/Si and Au(Pd)/Si(Ge) interfaces across the phase transition pressures up to 45 GPa. All data were measured at room temperature. Panels **a-d** are adapted with permission from Refs.[79,114,195,243], respectively. ©Springer Nature Publishers Limited. ©APS Publishers Limited.

5. Current applications

5.1 High-pressure high-temperature DAC simulations of materials in Earth's interior

Earth's core is under extreme conditions of high temperature about 6000 K and high pressure over 360 GPa at its center. Laser-heated DAC techniques provide the necessary and effective approaches for the Earth's interior exploration and simulation, by providing the relevant pressure-temperature conditions. A variety of coupled to DAC *in situ* probes such as XRD, X-ray absorption and Raman spectroscopy, TH, and TDTR[244-246] enable multiple experiments on the geoscience materials, such as the core and the mantle minerals, to study their physical and chemical properties, whereby contributing to understanding of the Earth's interior structure, composition, and evolution. Heat transport is crucial to clarify the thermal evolution and dynamics of the Earth's interior. A wealth of exploration works have been reported on the κ investigations of Earth's core, mantle, and core–mantle boundary materials through DAC experiments obtained at the corresponding high-pressure high-temperature conditions of Earth and first-principles calculations.[2,3,149,150,203,205,213] It is found that the adiabatic heat flux is 8-16 terawatts at the core–mantle boundary by computing the thermal and electrical conductivity in liquid mixtures at Earth's core conditions using first-principles calculations, higher than the previous estimates which are obtained based on the mantle convection.[2,247,248] To experimentally resolve this puzzle, the κ of iron-silicon alloys at Earth's core conditions was measured to be as low as 20 $Wm^{-1}K^{-1}$ through TDTR and TH experiments in DAC, suggesting a lower minimum heat flow of about 3 terawatts actually across the core–mantle boundary than previously expected.[60] In addition, the κ of solid iron at the Earth's core conditions via laser-heated DAC was measured within 18-44 $Wm^{-1}K^{-1}$; these values are near the low end of previous estimates and in agreement with palaeomagnetic measurements, indicating that the solid inner core has persisted since the beginning of Earth's history and as old as the dynamo.[3] Moreover, the κ of mantle minerals measured near the environment of lowermost mantle in DAC up to 120 GPa and 2500 K, revealed a value of ~3.9 $Wm^{-1}K^{-1}$ at 80 GPa and 2000-2500 K while ~5.9 $Wm^{-1}K^{-1}$ at 124 GPa and 2000-3000 K.[150] Therefore, these results further indicate that high-pressure

high-temperature experiments and simulations of Earth materials are important in the exploration of Earth's geodynamo and the prediction of Earth's evolution.

5.2 Strain modulation of thermoelectric performance

Thermoelectric materials not only can directly convert heat into electricity to fabricate generators according to Seebeck effect but also can utilize electricity for cooling to produce refrigerators based on Peltier effect. Since the discovery of the Seebeck effect in 1821, thermoelectric materials have witnessed hundreds of year's development and unveiled many high-performance systems such as bismuth telluride, lead chalcogenides, silicon-germanium, skutterudites, Zintl phases, and half-Heusler compounds.[67,249] Despite of these achievements, current thermoelectric materials are still too inefficient to achieve the goal of low-cost and large-scale applications in energy conversion. Thermoelectric performance, which can be assessed by the aforementioned zT formula, is overall determined by Seebeck coefficient, electrical conductivity, and thermal conductivity of materials. However, these physical quantities are mutually related, making them difficult to be modulated individually. To enhance the zT value, many approaches were adopted and some remarkable results were also obtained, such as band engineering,[250] nanostructuring strategies,[251] and strain modulation.[22,109] Particularly, strain modulation via pressure is found as a promising tool to improve the thermoelectric performance, which was recently confirmed by continued breakthroughs in examples of bismuth telluride,[252] lead chalcogenides,[22,253] ternary chalcopyrite,[109] half-Heusler compounds,[138] and so on. There are also many theoretical studies starting to focus on the enhancement of thermoelectric performance by pressure, which detailly illustrate and predict the evolution of the aforementioned three key parameters in thermoelectrics with respect to pressure.[254-256] In spite of these exciting efforts, there still lacks a comprehensive understanding and a universal mechanism on how the thermoelectric performance can be enhanced or modulated by pressure. One recent important finding is the pressure-induced electronic topological phase transition (TPT) interplayed with the closing and reopening of the band gap. The TPT is always accompanied by the anomalies of Seebeck coefficient and giant enhancement of electrical conductivity, resulting in the improvement of thermoelectric performance. This mechanism has been discovered well applied in bismuth telluride, lead selenide, and so on.[22,257,258] However, some materials like PdS, FeNbSb, $CuInTe_2$ are found that without undergoing such TPT, their thermoelectric performances were still improved under pressure; these phenomena were ascribed to the optimization of the carrier concentration and the band structure. In addition, the low-frequency Raman modes are found to be softened as the pressures are increased in PdS and $CuInTe_2$; this phonon softening can be correlated to a decrease in thermal conductivity.[109,138,139] Generally speaking, high-pressure technique has demonstrated its giant potential as a novel clean and effective strategy to optimize the thermoelectric performance.

6. Concluding remarks and outlook

Progressive achievements in high-pressure κ characterization techniques have allowed the in-depth understanding of heat transport, and uncovered many abnormal thermal phenomena and mechanisms that are hard to be probed at ambient conditions, as well as realized the reversible modulations of thermal conductivities of various materials. Guided by thermal transport theory, first-principles aided calculations have also predicted many unusual pressure-dependent κ behaviors that challenge the conventional thermal transport principles and provide promising chances for their practical thermal applications, however, these remain to be experimentally examined and physically illustrated.

Up to date, one of the greatest challenges for the κ characterization under pressure is that the size of samples loaded in the high-pressure apparatus is normally too small, making this the main difficulty faced in the measurements based on the present available methods. For example, in contact method using thermal couple and heater, the sample size needs to be larger than the thermal couple and the heater size, pushing the limited space within the DAC very challenging for this layout. Similar in the contactless method via optical approach, the sample size needs to be larger than the spot radius of the pump laser used in TDTR and TH methods, and the spot radius of the excitation laser used in Raman optothermal method; besides, the optical method further requires the samples' surfaces to be as smooth as possible, otherwise the optical signal would be seriously degraded by scattering. Another challenge is the measurement of in-plane thermal conductivity under pressure, or the anisotropic evolution of κ under pressure. Despite many reports to study the pressure-dependent κ, the outcomes are either isotropic or cross-plane thermal conductivity, while the interesting pressure-dependent in-plane thermal conductivity of abundant anisotropic materials remains unsolved. The in-plane thermal conductivity has broad theoretical utilities and practical applications in many anisotropic materials such as two-dimension materials and ultrathin films that are urgently needed for lateral heat spreading in electronics. Significant interests will be further raised if in-plane thermal conductivity modulation can be definitively realized and theoretically understood through methods of the strain modulation.

Furthermore, the κ modulation via strain method may steer new directions in development of electronics and devices for thermal management. Especially but not limited in electronic systems, intensity of heat density generation and the associated heat dissipation need to be fully understood and carefully conducted away, or the electronics will face significant temperature rise, likely leading to reliability challenges and possible failure. Take an example of the transistors, which is in the heart of the electronics industry. The tendency described by the Moore's law is related to successive shrinking of the device size to integrate a greater number of transistors to a more compacted chip, thus leading to dramatic power consumption increase in the integrated circuits; this brings a huge challenge in heat dissipation to ensure the device high performance and reliability. For instance, the heat flux generated at the local hotspot due to self-heating during the operation can exceed 1000 Wcm^{-2} in high

electron mobility transistors; this is a big threat to the device reliability and lifetime. From the view of thermal management, the total thermal resistance of devices needs to be greatly minimized. This consists of contribution from the κ and thickness of materials as well as the major hinder of ITC. It should be noted that in high power transistors, we expect larger κ; while in thermoelectrics lower κ values are desired. These contradictory details should be taken into account in thermal management design and this reminds us about the necessity to make careful considerations of the device purposes and requirements. In any case, both types of device applications would benefit from higher ITC to fast and efficiently conduct the heat across the interfaces. Presently, enhancing κ and ITC of materials are achieved mainly by improving the single-crystal materials quality with fewer defects, increasing the grain size of polycrystalline materials to reduce the grain boundary scattering, introducing high thermal conducting interfacial materials or integrating with diamond like high κ materials. Besides of the above ambient methods, strain or pressure can also be used to tune the κ of materials and the ITC at interfaces, despite this part of research is still in its infant stage due to the challenges of high-pressure thermal characterization techniques; however, this method may inform novel thermal management techniques in electronic devices.

In this Review, we have provided a systematic discussion of the progress related to the thermal properties' evolution under pressure, summarizing the behaviors of a variety of materials from gases, liquids to solids and solid-solid interfaces that have been investigated, as well as the thermal characterization methodological developments and some interesting theoretical predictions. Exciting application examples of thermo-physical properties characterization of minerals at high pressure and high temperature that are important in modelling thermal evolution of the deep Earth's mantle/core conditions, and thermal conductivity modulations in thermoelectrics by pressure are also introduced. Knowledge about the pressure dependence of thermal conductivity has opened new physical insights into the nature of phonon scattering and thermal transport from a new dimension, and extended the thermal modulation ability, especially when in combination with the temperature. Furthermore, a promising outlook in theoretical and experimental investigations of various high-pressure thermal properties and related thermal management techniques is also discussed. An additional viewpoint, which is worth to note, is that improving the reliability and precision in determining the pressure dependent thermo-physical properties require further implementation of advanced characterization techniques. Presently, defying the small size and very narrow space of diamond anvil cell tools, all-optical laser thermoreflectance, transient heating, and opto-thermal fast contactless experimental techniques have attracted more and more interests, and displayed great potential in future developments, although there are still lots of unknowns need to be explored and improved in these methods.

References

1. Ohta, K. *et al.* The electrical conductivity of post-perovskite in Earth's D'' layer. *Science* **320**,

89-91 (2008).
2. Pozzo, M., Davies, C., Gubbins, D. & Alfè, D. Thermal and electrical conductivity of iron at Earth's core conditions. *Nature* **485**, 355-358 (2012).
3. Konôpková, Z., McWilliams, R. S., Gómez-Pérez, N. & Goncharov, A. F. Direct measurement of thermal conductivity in solid iron at planetary core conditions. *Nature* **534**, 99-101 (2016).
4. Ohta, K., Kuwayama, Y., Hirose, K., Shimizu, K. & Ohishi, Y. Experimental determination of the electrical resistivity of iron at Earth's core conditions. *Nature* **534**, 95-98 (2016).
5. Knudson, M. D. *et al.* Direct observation of an abrupt insulator-to-metal transition in dense liquid deuterium. *Science* **348**, 1455-1460 (2015).
6. Celliers, P. M. *et al.* Insulator-metal transition in dense fluid deuterium. *Science* **361**, 677-682 (2018).
7. Eremets, M. I., Drozdov, A. P., Kong, P. & Wang, H. Semimetallic molecular hydrogen at pressure above 350 GPa. *Nat. Phys.* **15**, 1246-1249 (2019).
8. Ji, C. *et al.* Ultrahigh-pressure isostructural electronic transitions in hydrogen. *Nature* **573**, 558-562 (2019).
9. Cheng, B., Mazzola, G., Pickard, C. J. & Ceriotti, M. Evidence for supercritical behaviour of high-pressure liquid hydrogen. *Nature* **585**, 217-220 (2020).
10. Jiang, S. *et al.* A spectroscopic study of the insulator–metal transition in liquid hydrogen and deuterium. *Adv. Sci.* **7**, 1901668 (2020).
11. Mao, H.-K., Chen, X.-J., Ding, Y., Li, B. & Wang, L. Solids, liquids, and gases under high pressure. *Rev. Mod. Phys.* **90**, 015007 (2018).
12. Zhang, L., Wang, Y., Lv, J. & Ma, Y. Materials discovery at high pressures. *Nat. Rev. Mater.* **2**, 17005 (2017).
13. Miao, M., Sun, Y., Zurek, E. & Lin, H. Chemistry under high pressure. *Nat. Rev. Chem.* **4**, 508-527 (2020).
14. Hofmeister, A. M. Pressure dependence of thermal transport properties. *Proc. Natl. Acad. Sci. USA* **104**, 9192-9197 (2007).
15. Drozdov, A., Eremets, M., Troyan, I., Ksenofontov, V. & Shylin, S. I. Conventional superconductivity at 203 kelvin at high pressures in the sulfur hydride system. *Nature* **525**, 73-76 (2015).
16. Drozdov, A. *et al.* Superconductivity at 250 K in lanthanum hydride under high pressures. *Nature* **569**, 528-531 (2019).
17. Somayazulu, M. *et al.* Evidence for superconductivity above 260 K in lanthanum superhydride at megabar pressures. *Phys. Rev. Lett.* **122**, 027001 (2019).
18. Snider, E. *et al.* Room-temperature superconductivity in a carbonaceous sulfur hydride. *Nature* **586**, 373-377 (2020).
19. Medvedev, S. *et al.* Electronic and magnetic phase diagram of β-$Fe_{1.01}Se$ with superconductivity at 36.7 K under pressure. *Nat. Mater.* **8**, 630-633 (2009).
20. Chen, X.-J. *et al.* Enhancement of superconductivity by pressure-driven competition in electronic order. *Nature* **466**, 950-953 (2010).
21. Sun, L. *et al.* Re-emerging superconductivity at 48 kelvin in iron chalcogenides. *Nature* **483**, 67-69 (2012).
22. Chen, L.-C. *et al.* Enhancement of thermoelectric performance across the topological

phase transition in dense lead selenide. *Nat. Mater.* **18**, 1321-1326 (2019).
23. Chi, Z.-H. *et al.* Pressure-induced metallization of molybdenum disulfide. *Phys. Rev. Lett.* **113**, 036802 (2014).
24. Zhao, X.-M. *et al.* Pressure tuning of the charge density wave and superconductivity in 2*H*-TaS_2. *Phys. Rev. B* **101**, 134506 (2020).
25. Mao, H. K. High-pressure physics: Sustained static generation of 1.36 to 1.72 megabars. *Science* **200**, 1145-1147 (1978).
26. Mao, H. K. & Bell, P. M. High-pressure physics: The 1-megabar mark on the ruby R_1 static pressure scale. *Science* **191**, 851-852 (1976).
27. Jayaraman, A. Diamond anvil cell and high-pressure physical investigations. *Rev. Mod. Phys.* **55**, 65-108 (1983).
28. Wang, L. *et al.* Nanoprobe measurements of materials at megabar pressures. *Proc. Natl. Acad. Sci. USA* **107**, 6140-6145 (2010).
29. Dubrovinsky, L., Dubrovinskaia, N., Prakapenka, V. B. & Abakumov, A. M. Implementation of micro-ball nanodiamond anvils for high-pressure studies above 6 Mbar. *Nat. Commun.* **3**, 1163 (2012).
30. Irifune, T., Kunimoto, T., Shinmei, T. & Tange, Y. High pressure generation in Kawai-type multianvil apparatus using nano-polycrystalline diamond anvils. *Comptes Rendus Geoscience* **351**, 260-268 (2019).
31. Liebermann, R. C. Multi-anvil, high pressure apparatus: a half-century of development and progress. *High Press. Res.* **31**, 493-532 (2011).
32. Dubrovinsky, L. *et al.* The most incompressible metal osmium at static pressures above 750 gigapascals. *Nature* **525**, 226-229 (2015).
33. Barker Jr, R. & Chen, R. Grüneisen parameter from thermal conductivity measurements under pressure. *J. Chem. Phys.* **53**, 2616-2620 (1970).
34. Walker, I. Nonmagnetic piston–cylinder pressure cell for use at 35 kbar and above. *Rev. Sci. Instrum.* **70**, 3402-3412 (1999).
35. Mao, H. K., Xu, J. & Bell, P. M. Calibration of the ruby pressure gauge to 800 kbar under quasi-hydrostatic conditions. *J. Geophys. Res.* **91**, 4673-4676 (1986).
36. Akahama, Y. & Kawamura, H. Pressure calibration of diamond anvil Raman gauge to 410 GPa. *J. Phys. Conf. Ser.* **215**, 012195 (2010).
37. Livneh, T. & Sterer, E. Resonant Raman scattering at exciton states tuned by pressure and temperature in 2H-MoS_2. *Phys. Rev. B* **81**, 195209 (2010).
38. Beck, P. *et al.* Measurement of thermal diffusivity at high pressure using a transient heating technique. *Appl. Phys. Lett.* **91**, 181914 (2007).
39. Hsieh, W.-P., Chen, B., Li, J., Keblinski, P. & Cahill, D. G. Pressure tuning of the thermal conductivity of the layered muscovite crystal. *Phys. Rev. B* **80**, 180302 (2009).
40. Wang, Y. *et al.* Pressure-induced phase transformation, reversible amorphization, and anomalous visible light response in organolead bromide perovskite. *J. Am. Chem. Soc.* **137**, 11144-11149 (2015).
41. Conley, H. J. *et al.* Bandgap engineering of strained monolayer and bilayer MoS_2. *Nano Lett.* **13**, 3626-3630 (2013).
42. Bertolazzi, S., Brivio, J. & Kis, A. Stretching and breaking of ultrathin MoS_2. *ACS Nano* **5**, 9703-9709 (2011).

43. Wang, Y. *et al.* Strain-induced direct–indirect bandgap transition and phonon modulation in monolayer WS_2. *Nano Res.* **8**, 2562-2572 (2015).
44. Wu, W. *et al.* Giant mechano-optoelectronic effect in an atomically thin semiconductor. *Nano Lett.* **18**, 2351-2357 (2018).
45. He, K., Poole, C., Mak, K. F. & Shan, J. Experimental demonstration of continuous electronic structure tuning via strain in atomically thin MoS_2. *Nano Lett.* **13**, 2931-2936 (2013).
46. Rice, C. *et al.* Raman-scattering measurements and first-principles calculations of strain-induced phonon shifts in monolayer MoS_2. *Phys. Rev. B* **87**, 081307 (2013).
47. Wang, Y., Cong, C., Qiu, C. & Yu, T. Raman spectroscopy study of lattice vibration and crystallographic orientation of monolayer MoS_2 under uniaxial strain. *Small* **9**, 2857-2861 (2013).
48. Ci, P. *et al.* Quantifying van der Waals interactions in layered transition metal dichalcogenides from pressure-enhanced valence band splitting. *Nano Lett.* **17**, 4982-4988 (2017).
49. Meng, X. *et al.* Thermal conductivity enhancement in MoS_2 under extreme strain. *Phys. Rev. Lett.* **122**, 155901 (2019).
50. Howie, R. T., Magdău, I. B., Goncharov, A. F., Ackland, G. J. & Gregoryanz, E. Phonon localization by mass disorder in dense hydrogen-deuterium binary alloy. *Phys. Rev. Lett.* **113**, 175501 (2014).
51. Howie, R. T., Dalladay-Simpson, P. & Gregoryanz, E. Raman spectroscopy of hot hydrogen above 200 GPa. *Nat. Mater.* **14**, 495-499 (2015).
52. Dalladay-Simpson, P., Howie, R. T. & Gregoryanz, E. Evidence for a new phase of dense hydrogen above 325 gigapascals. *Nature* **529**, 63-67 (2016).
53. Li, F. *et al.* Brillouin scattering spectroscopy for a laser heated diamond anvil cell. *Appl. Phys. Lett.* **88**, 203507 (2006).
54. Nayak, A. P. *et al.* Pressure-induced semiconducting to metallic transition in multilayered molybdenum disulphide. *Nat. Commun.* **5**, 3731 (2014).
55. Chi, Z. *et al.* Superconductivity in pristine $2H_a$–MoS_2 at ultrahigh pressure. *Phys. Rev. Lett.* **120**, 037002 (2018).
56. Mao, W. L. *et al.* Bonding changes in compressed superhard graphite. *Science* **302**, 425-427 (2003).
57. Li, Q. *et al.* Superhard monoclinic polymorph of carbon. *Phys. Rev. Lett.* **102**, 175506 (2009).
58. Tian, Y. *et al.* Ultrahard nanotwinned cubic boron nitride. *Nature* **493**, 385-388 (2013).
59. Huang, Q. *et al.* Nanotwinned diamond with unprecedented hardness and stability. *Nature* **510**, 250-253 (2014).
60. Hsieh, W.-P. *et al.* Low thermal conductivity of iron-silicon alloys at Earth's core conditions with implications for the geodynamo. *Nat. Commun.* **11**, 3332 (2020).
61. Chen, X.-J. *et al.* Pressure-induced phonon frequency shifts in transition-metal nitrides. *Phys. Rev. B* **70**, 014501 (2004).
62. Ma, Z. *et al.* Pressure-induced emission of cesium lead halide perovskite nanocrystals. *Nat. Commun.* **9**, 4506 (2018).
63. Li, M., Liu, T., Wang, Y., Yang, W. & Lü, X. Pressure responses of halide perovskites with

various compositions, dimensionalities, and morphologies. *Matter Radiat. Extremes* **5**, 018201 (2020).
64. Cahill, D. G. *et al.* Nanoscale thermal transport. *J. Appl. Phys.* **93**, 793-818 (2003).
65. Cahill, D. G. *et al.* Nanoscale thermal transport. II. 2003–2012. *Appl. Phys. Rev.* **1**, 011305 (2014).
66. Giri, A. & Hopkins, P. E. A review of experimental and computational advances in thermal boundary conductance and nanoscale thermal transport across solid interfaces. *Adv. Funct. Mater.* **30**, 1903857 (2020).
67. Snyder, G. J. & Toberer, E. S. Complex thermoelectric materials. *Nat. Mater.* **7**, 105-114 (2008).
68. Huxtable, S. T., Cahill, D. G. & Phinney, L. M. Thermal contact conductance of adhered microcantilevers. *J. Appl. Phys.* **95**, 2102-2108 (2004).
69. Kaviany, M. *Heat transfer physics* (Cambridge University Press, 2014).
70. Chen, S. *et al.* Thermal conductivity of isotopically modified graphene. *Nat. Mater.* **11**, 203-207 (2012).
71. Li, X., Maute, K., Dunn, M. L. & Yang, R. Strain effects on the thermal conductivity of nanostructures. *Phys. Rev. B* **81**, 245318 (2010).
72. Ding, Z., Pei, Q.-X., Jiang, J.-W. & Zhang, Y.-W. Manipulating the thermal conductivity of monolayer MoS_2 via lattice defect and strain engineering. *J. Phys. Chem. C* **119**, 16358-16365 (2015).
73. Wei, Z., Chen, Y. & Dames, C. Negative correlation between in-plane bonding strength and cross-plane thermal conductivity in a model layered material. *Appl. Phys. Lett.* **102**, 011901 (2013).
74. Lindsay, L., Broido, D. A., Carrete, J., Mingo, N. & Reinecke, T. L. Anomalous pressure dependence of thermal conductivities of large mass ratio compounds. *Phys. Rev. B* **91**, 121202 (2015).
75. Ouyang, T. & Hu, M. Competing mechanism driving diverse pressure dependence of thermal conductivity of *X*Te (*X*=Hg, Cd, and Zn). *Phys. Rev. B* **92**, 235204 (2015).
76. Ravichandran, N. K. & Broido, D. Non-monotonic pressure dependence of the thermal conductivity of boron arsenide. *Nat. Commun.* **10**, 827 (2019).
77. Ross, R. G., Andersson, P., Sundqvist, B. & Backstrom, G. Thermal conductivity of solids and liquids under pressure. *Rep. Prog. Phys.* **47**, 1347-1402 (1984).
78. Chen, J., Walther, J. H. & Koumoutsakos, P. Strain engineering of Kapitza resistance in few-layer graphene. *Nano Lett.* **14**, 819-825 (2014).
79. Hohensee, G. T., Wilson, R. & Cahill, D. G. Thermal conductance of metal–diamond interfaces at high pressure. *Nat. Commun.* **6**, 6578 (2015).
80. Vandersande, J. & Wood, C. The thermal conductivity of insulators and semiconductors. *Contemp. Phys.* **27**, 117-144 (1986).
81. Wang, Y., Qiu, B., J. H. McGaughey, A., Ruan, X. & Xu, X. Mode-wise thermal conductivity of bismuth telluride. *J. Heat Transfer* **135**, 091102 (2013).
82. Borca-Tasciuc, D.-A. *et al.* Thermal properties of electrodeposited bismuth telluride nanowires embedded in amorphous alumina. *Appl. Phys. Lett.* **85**, 6001-6003 (2004).
83. Mavrokefalos, A. *et al.* Thermoelectric and structural characterizations of individual electrodeposited bismuth telluride nanowires. *J. Appl. Phys.* **105**, 104318 (2009).

84. Park, K. H., Mohamed, M., Aksamija, Z. & Ravaioli, U. Phonon scattering due to van der Waals forces in the lattice thermal conductivity of Bi_2Te_3 thin films. *J. Appl. Phys.* **117**, 015103 (2015).
85. Al-Alam, P. *et al.* Lattice thermal conductivity of Bi_2Te_3 and SnSe using Debye-Callaway and Monte Carlo phonon transport modeling: Application to nanofilms and nanowires. *Phys. Rev. B* **100**, 115304 (2019).
86. Prasher, R. Acoustic mismatch model for thermal contact resistance of van der Waals contacts. *Appl. Phys. Lett.* **94**, 041905 (2009).
87. Huang, B.-L. & Kaviany, M. Ab initio and molecular dynamics predictions for electron and phonon transport in bismuth telluride. *Phys. Rev. B* **77**, 125209 (2008).
88. Qiu, B. & Ruan, X. Molecular dynamics simulations of lattice thermal conductivity of bismuth telluride using two-body interatomic potentials. *Phys. Rev. B* **80**, 165203 (2009).
89. Termentzidis, K. *et al.* Large thermal conductivity decrease in point defective Bi_2Te_3 bulk materials and superlattices. *J. Appl. Phys.* **113**, 013506 (2013).
90. Kapitza, P. L. Heat transfer and superfluidity of helium II. *Phys. Rev.* **60**, 354-355 (1941).
91. Pop, E. Energy dissipation and transport in nanoscale devices. *Nano Res.* **3**, 147-169 (2010).
92. Kuball, M. & Pomeroy, J. W. A review of raman thermography for electronic and opto-electronic device measurement with submicron spatial and nanosecond temporal resolution. *IEEE Trans. Device Mater. Reliab.* **16**, 667-684 (2016).
93. Siegrist, T., Merkelbach, P. & Wuttig, M. Phase change materials: Challenges on the path to a universal storage device. *Annu. Rev. Condens. Matter Phys.* **3**, 215-237 (2012).
94. Wuttig, M., Bhaskaran, H. & Taubner, T. Phase-change materials for non-volatile photonic applications. *Nat. Photonics* **11**, 465-476 (2017).
95. Costescu, R. M., Cahill, D. G., Fabreguette, F. H., Sechrist, Z. A. & George, S. M. Ultra-low thermal conductivity in W/Al_2O_3 nanolaminates. *Science* **303**, 989-990 (2004).
96. Losego, M. D., Blitz, I. P., Vaia, R. A., Cahill, D. G. & Braun, P. V. Ultralow thermal conductivity in organoclay nanolaminates synthesized via simple self-assembly. *Nano Lett.* **13**, 2215-2219 (2013).
97. Giri, A., Donovan, B. F. & Hopkins, P. E. Localization of vibrational modes leads to reduced thermal conductivity of amorphous heterostructures. *Phys. Rev. Mater.* **2**, 056002 (2018).
98. Merabia, S., Shenogin, S., Joly, L., Keblinski, P. & Barrat, J.-L. Heat transfer from nanoparticles: A corresponding state analysis. *Proc. Natl. Acad. Sci. USA* **106**, 15113-15118 (2009).
99. Little, W. The transport of heat between dissimilar solids at low temperatures. *Can. J. Phys.* **37**, 334-349 (1959).
100. Swartz, E. & Pohl, R. Thermal resistance at interfaces. *Appl. Phys. Lett.* **51**, 2200-2202 (1987).
101. Swartz, E. T. & Pohl, R. O. Thermal boundary resistance. *Rev. Mod. Phys.* **61**, 605-668 (1989).
102. Stoner, R. & Maris, H. Kapitza conductance and heat flow between solids at temperatures from 50 to 300 K. *Phys. Rev. B* **48**, 16373-16387 (1993).
103. Stevens, R. J., Smith, A. N. & Norris, P. M. Measurement of thermal boundary conductance of a series of metal-dielectric interfaces by the transient thermoreflectance

technique. *J. Heat Transfer* **127**, 315-322 (2005).
104. Snyder, N. Heat transport through helium II: Kapitza conductance. *Cryogenics* **10**, 89-95 (1970).
105. Lyeo, H.-K. & Cahill, D. G. Thermal conductance of interfaces between highly dissimilar materials. *Phys. Rev. B* **73**, 144301 (2006).
106. Hopkins, P. E., Norris, P. M. & Stevens, R. J. Influence of inelastic scattering at metal-dielectric interfaces. *J. Heat Transfer* **130**, 022401 (2008).
107. Stevens, R. J., Zhigilei, L. V. & Norris, P. M. Effects of temperature and disorder on thermal boundary conductance at solid–solid interfaces: Nonequilibrium molecular dynamics simulations. *International Journal of Heat and Mass Transfer* **50**, 3977-3989 (2007).
108. Sun, Z., Yuan, K., Zhang, X. & Tang, D. Pressure tuning of the thermal conductivity of gallium arsenide from first-principles calculations. *Phys. Chem. Chem. Phys.* **20**, 30331-30339 (2018).
109. Yu, H. *et al.* Large enhancement of thermoelectric performance in $CuInTe_2$ upon compression. *Mater. Today Phys.* **5**, 1-6 (2018).
110. Wang, L. *et al.* High-pressure phases of boron arsenide with potential high thermal conductivity. *Phys. Rev. B* **99**, 174104 (2019).
111. Saha, P., Mazumder, A. & Mukherjee, G. D. Thermal conductivity of dense hcp iron: Direct measurements using laser heated diamond anvil cell. *Geosci. Front.* ***11***, 1755-1761 (2020).
112. Yuan, K., Zhang, X., Tang, D. & Hu, M. Anomalous pressure effect on the thermal conductivity of ZnO, GaN, and AlN from first-principles calculations. *Phys. Rev. B* **98**, 144303 (2018).
113. Lan, G., Ouyang, B. & Song, J. The role of low-lying optical phonons in lattice thermal conductance of rare-earth pyrochlores: A first-principle study. *Acta Mater.* **91**, 304-317 (2015).
114. Hsieh, W.-P., Lyons, A. S., Pop, E., Keblinski, P. & Cahill, D. G. Pressure tuning of the thermal conductance of weak interfaces. *Phys. Rev. B* **84**, 184107 (2011).
115. Fujisawa, H., Fujii, N., Mizutani, H., Kanamori, H. & Akimoto, S. i. Thermal diffusivity of Mg_2SiO_4, Fe_2SiO_4, and NaCl at high pressures and temperatures. *J. Geophys. Res.* **73**, 4727-4733 (1968).
116. Håkansson, B., Andersson, P. & Bäckström, G. Improved hot-wire procedure for thermophysical measurements under pressure. *Rev. Sci. Instrum.* **59**, 2269-2275 (1988).
117. Katsura, T. Thermal diffusivity of silica glass at pressures up to 9 GPa. *Phys. Chem. Miner.* **20**, 201-208 (1993).
118. Xu, Y. *et al.* Thermal diffusivity and conductivity of olivine, wadsleyite and ringwoodite to 20 GPa and 1373 K. *Phys. Earth Planet. Inter.* **143-144**, 321-336 (2004).
119. Bercegeay, C. & Bernard, S. First-principles equations of state and elastic properties of seven metals. *Phys. Rev. B* **72**, 214101 (2005).
120. Hsieh, W.-P. *et al.* Testing the minimum thermal conductivity model for amorphous polymers using high pressure. *Phys. Rev. B* **83**, 174205 (2011).
121. Park, C. H., Cheong, B.-H., Lee, K.-H. & Chang, K. J. Structural and electronic properties of cubic, 2H, 4H, and 6H SiC. *Phys. Rev. B* **49**, 4485-4493 (1994).

122. Zha, C.-S., Mao, H.-k. & Hemley, R. J. Elasticity of MgO and a primary pressure scale to 55 GPa. *Proc. Natl. Acad. Sci. USA* **97**, 13494-13499 (2000).
123. Xie, J., Chen, S. P., Tse, J. S., Gironcoli, S. d. & Baroni, S. High-pressure thermal expansion, bulk modulus, and phonon structure of diamond. *Phys. Rev. B* **60**, 9444-9449 (1999).
124. Barker Jr, R., Chen, R. & Frost, R. Influence of pressure and chemical structure on the thermal conductivity of vitreous poly (alkyl methacrylates). I. *J. Polym. Sci: Polym. Phys.* **15**, 1199-1210 (1977).
125. Hsieh, W.-P. *Testing theories for thermal transport using high pressure*, University of Illinois at Urbana-Champaign (2012).
126. Frost, R. S., Chen, R. Y. S. & Barker Jr., R. E. Pressure dependence of thermal conductivity in polyethylene. *J. Appl. Phys.* **46**, 4506-4509 (1975).
127. Manthilake, M. A. G. M., de Koker, N. & Frost, D. J. Thermal conductivity of $CaGeO_3$ perovskite at high pressure. *Geophys. Res. Lett.* **38**, L038301 (2011).
128. Frost, D. J. *et al.* A new large-volume multianvil system. *Phys. Earth Planet. Inter.* **143-144**, 507-514 (2004).
129. Katsura, T. Thermal diffusivity of olivine under upper mantle conditions. *Geophys. J. Int.* **122**, 63-69 (1995).
130. Manthilake, G. M., de Koker, N., Frost, D. J. & McCammon, C. A. Lattice thermal conductivity of lower mantle minerals and heat flux from Earth's core. *Proc. Natl. Acad. Sci. USA* **108**, 17901 (2011).
131. Chai, M., Brown, J. M. & Slutsky, L. J. Thermal diffusivity of mantle minerals. *Phys. Chem. Miner.* **23**, 470-475 (1996).
132. Yue, D. *et al.* Accurate temperature measurement by temperature field analysis in diamond anvil cell for thermal transport study of matter under high pressures. *Appl. Phys. Lett.* **112**, 081901 (2018).
133. Franco, A. An apparatus for the routine measurement of thermal conductivity of materials for building application based on a transient hot-wire method. *Appl. Therm. Eng.* **27**, 2495-2504 (2007).
134. Goncharov, A. F., Beck, P., Struzhkin, V. V., Haugen, B. D. & Jacobsen, S. D. Thermal conductivity of lower-mantle minerals. *Phys. Earth Planet. Inter.* **174**, 24-32 (2009).
135. McWilliams, R. S., Konôpková, Z. & Goncharov, A. F. A flash heating method for measuring thermal conductivity at high pressure and temperature: Application to Pt. *Phys. Earth Planet. Inter.* **247**, 17-26 (2015).
136. Abramson, E. H., Brown, J. M. & Slutsky, L. J. The thermal diffusivity of water at high pressures and temperatures. *J. Chem. Phys.* **115**, 10461-10463 (2001).
137. Abramson, E. H., Slutsky, L. J. & Brown, J. M. Thermal diffusivity of fluid oxygen to 12 GPa and 300 °C. *J. Chem. Phys.* **111**, 9357-9360 (1999).
138. Pang, H.-J. *et al.* Pressure tuning of thermoelectric performance in FeNbSb. *J. Alloys Compd.* **805**, 1224-1230 (2019).
139. Chen, L.-C. *et al.* Pressure-induced enhancement of thermoelectric performance in palladium sulfide. *Mater. Today Phys.* **5**, 64-71 (2018).
140. Håkansson, B. & Ross, R. G. Effective thermal conductivity of binary dispersed composites over wide ranges of volume fraction, temperature, and pressure. *J. Appl. Phys.* **68**, 3285-3292 (1990).

141. Andersson, O. & Suga, H. Thermal conductivity of the Ih and XI phases of ice. *Phys. Rev. B* **50**, 6583-6588 (1994).
142. Andersson, O. & Suga, H. Thermal conductivity of normal and deuterated tetrahydrofuran clathrate hydrates. *J. Phys. Chem. Solids* **57**, 125-132 (1996).
143. Andersson, O., Soldatov, A. & Sundqvist, B. Thermal conductivity of C_{60} at pressures up to 1 GPa and temperatures in the 50-300 K range. *Phys. Rev. B* **54**, 3093-3100 (1996).
144. Larsson, R. & Andersson, O. Lubricant thermal conductivity and heat capacity under high pressure. *Proceedings of the Institution of Mechanical Engineers, Part J: Journal of Engineering Tribology* **214**, 337-342 (2000).
145. Andersson, O., Chobal, O., Rizak, I., Rizak, V. & Sabadosh, V. Effects of pressure and temperature on the thermal conductivity of $Sn_2P_2S_6$. *Phys. Rev. B* **83**, 134121 (2011).
146. Yu, J., Tonpheng, B., Gröbner, G. & Andersson, O. Thermal properties and transition studies of multi-wall carbon nanotube/nylon-6 composites. *Carbon* **49**, 4858-4866 (2011).
147. Andersson, O. Thermal conductivity of normal and deuterated water, crystalline ice, and amorphous ices. *J. Chem. Phys.* **149**, 124506 (2018).
148. Soldatov, A. & Sundqvist, B. Molecular rotation in C_{70} at high pressures: A thermal conductivity study. *J. Phys. Chem. Solids* **57**, 1371-1375 (1996).
149. Goncharov, A. F. *et al.* Effect of composition, structure, and spin state on the thermal conductivity of the Earth's lower mantle. *Phys. Earth Planet. Inter.* **180**, 148-153 (2010).
150. Geballe, Z. M., Sime, N., Badro, J., van Keken, P. E. & Goncharov, A. F. Thermal conductivity near the bottom of the Earth's lower mantle: Measurements of pyrolite up to 120 GPa and 2500 K. E*arth Planet. Sci. Lett.* **536**, 116161 (2020).
151. Chiritescu, C. *et al.* Ultralow thermal conductivity in disordered, layered WSe_2 crystals. *Science* **315**, 351-353 (2007).
152. Ge, Z., Cahill, D. G. & Braun, P. V. Thermal conductance of hydrophilic and hydrophobic interfaces. *Phys. Rev. Lett.* **96**, 186101 (2006).
153. Beran, A. The reflectance behaviour of gold at temperatures up to 500 °C. *Tschermaks Mineralogische und Petrographische Mitteilungen* **34**, 211-215 (1985).
154. Hsieh, W.-P. & Cahill, D. G. Ta and Au(Pd) alloy metal film transducers for time-domain thermoreflectance at high pressures. *J. Appl. Phys.* **109**, 113520 (2011).
155. Hsieh, W.-P. Thermal conductivity of methanol-ethanol mixture and silicone oil at high pressures. *J. Appl. Phys.* **117**, 235901 (2015).
156. Jeong, J. *et al.* Picosecond transient thermoreflectance for thermal conductivity characterization. *Nanoscale Microscale Thermophys. Eng.* **23**, 211-221 (2019).
157. Hasegawa, A., Yagi, T. & Ohta, K. Combination of pulsed light heating thermoreflectance and laser-heated diamond anvil cell for in-situ high pressure-temperature thermal diffusivity measurements. *Rev. Sci. Instrum.* **90**, 074901 (2019).
158. Omini, M. & Sparavigna, A. An iterative approach to the phonon Boltzmann equation in the theory of thermal conductivity. *Physica B: Condens. Matter* **212**, 101-112 (1995).
159. Fugallo, G., Lazzeri, M., Paulatto, L. & Mauri, F. Ab initio variational approach for evaluating lattice thermal conductivity. *Phys. Rev. B* **88**, 045430 (2013).
160. Stillinger, F. H. & Weber, T. A. Computer simulation of local order in condensed phases of silicon. *Phys. Rev. B* **31**, 5262-5271 (1985).
161. Tersoff, J. Empirical interatomic potential for carbon, with applications to amorphous

carbon. *Phys. Rev. Lett.* **61**, 2879-2882 (1988).
162. Brenner, D. W. Empirical potential for hydrocarbons for use in simulating the chemical vapor deposition of diamond films. *Phys. Rev. B* **42**, 9458-9471 (1990).
163. Weber, W. Adiabatic bond charge model for the phonons in diamond, Si, Ge, and α−Sn. *Phys. Rev. B* **15**, 4789-4803 (1977).
164. Broido, D. A., Malorny, M., Birner, G., Mingo, N. & Stewart, D. A. Intrinsic lattice thermal conductivity of semiconductors from first principles. *Appl. Phys. Lett.* **91**, 231922 (2007).
165. Lindsay, L. First principles Peierls-Boltzmann phonon thermal transport: A topical review. *Nanoscale Microscale Thermophys. Eng.* **20**, 67-84 (2016).
166. de Koker, N. Thermal conductivity of MgO periclase from equilibrium first principles molecular dynamics. *Phys. Rev. Lett.* **103**, 125902 (2009).
167. Tian, F. *et al.* Unusual high thermal conductivity in boron arsenide bulk crystals. *Science* **361**, 582-585 (2018).
168. Ravichandran, N. K. & Broido, D. Unified first-principles theory of thermal properties of insulators. *Phys. Rev. B* **98**, 085205 (2018).
169. Hamrin, C. E. & Thodos, G. The thermal conductivity of hydrogen for pressures up to 660 atm and temperatures between 1.6 and 74.6 °C. *Physica* **32**, 918-932 (1966).
170. Roder, H. M. The thermal conductivity of oxygen. *J. Res.* **87**, 279-310 (1982).
171. Roder, H. M. Thermal conductivity of methane for temperatures between 110 and 310 K with pressures to 70 MPa. *Int. J. Thermophys.* **6**, 119-142 (1985).
172. Gilmore, T. F. & Comings, E. W. Thermal conductivity of binary mixtures of carbon dioxide, nitrogen, and ethane at high pressures: Comparison with correlation and theory. *AIChE Journal* **12**, 1172-1178 (1966).
173. Sengers, J. V., Bolk, W. T. & Stigter, C. J. The thermal conductivity of neon between 25 °C and 75 °C at pressures up to 2600 atmospheres. *Physica* **30**, 1018-1026 (1964).
174. Millat, J., Mustafa, M., Ross, M., Wakeham, W. A. & Zalaf, M. The thermal conductivity of argon, carbon dioxide and nitrous oxide. *Physica A: Statistical Mechanics and its Applications* **145**, 461-497 (1987).
175. Goncharov, A. F. *et al.* Thermal conductivity of argon at high pressures and high temperatures. *J. Appl. Phys.* **111**, 112609 (2012).
176. Tretiakov, K. V. & Scandolo, S. Thermal conductivity of solid argon at high pressure and high temperature: A molecular dynamics study. *J. Chem. Phys.* **121**, 11177-11182 (2004).
177. Chernatynskiy, A. & Phillpot, S. R. Thermal conductivity of argon at high pressure from first principles calculations. *J. Appl. Phys.* **114**, 064902 (2013).
178. Michels, A., Sengers, J. V. & Van De Klundert, L. J. M. The thermal conductivity of argon at elevated densities. *Physica* **29**, 149-160 (1963).
179. Parrish, K. D., Jain, A., Larkin, J. M., Saidi, W. A. & McGaughey, A. J. H. Origins of thermal conductivity changes in strained crystals. *Phys. Rev. B* **90**, 235201 (2014).
180. Johns, A. I., Rashid, S., Rowan, L., Watson, J. T. R. & Clifford, A. A. The thermal conductivity of pure nitrogen and of mixtures of nitrogen and carbon dioxide at elevated temperatures and pressures. *Int. J. Thermophys.* **9**, 3-19 (1988).
181. Moroe, S. *et al.* Measurements of hydrogen thermal conductivity at high pressure and high temperature. *Int. J. Thermophys.* **32**, 1887-1917 (2011).
182. Shulga, V. M., Eldarov, F. G., Atanov, Y. A. & Kuyumchev, A. A. Thermal conductivity and

heat capacity of liquid toluene at temperatures between 255 and 400 K and at pressures up to 1000 MPa. *Int. J. Thermophys.* **7**, 1147-1161 (1986).

183. Ramaswamy, R., Balasubramaniam, V. M. & Sastry, S. K. Thermal conductivity of selected liquid foods at elevated pressures up to 700 MPa. *J. Food Eng.* **83**, 444-451 (2007).

184. Chen, B., Hsieh, W.-P., Cahill, D. G., Trinkle, D. R. & Li, J. Thermal conductivity of compressed H_2O to 22 GPa: A test of the Leibfried-Schlomann equation. *Phys. Rev. B* **83**, 132301 (2011).

185. Ross, R. G., Andersson, P. & Bäckström, G. Thermal conductivity of allotropic modifications of ice. *Nature* **259**, 553-554 (1976).

186. Hsieh, W.-P., Deschamps, F., Okuchi, T. & Lin, J.-F. Effects of iron on the lattice thermal conductivity of Earth's deep mantle and implications for mantle dynamics. *Proc. Natl. Acad. Sci. USA* **115**, 4099-4104 (2018).

187. Hsieh, W. P., Deschamps, F., Okuchi, T. & Lin, J. F. Reduced lattice thermal conductivity of Fe-bearing bridgmanite in Earth's deep mantle. *J. Geophys. Res.: Solid Earth* **122**, 4900-4917 (2017).

188. Chao, K.-H. & Hsieh, W.-P. Thermal conductivity anomaly in $(Fe_{0.78}Mg_{0.22})CO_3$ siderite across spin transition of iron. *J. Geophys. Res.: Solid Earth* **124**, 1388-1396 (2019).

189. Dalton, D. A., Hsieh, W.-P., Hohensee, G. T., Cahill, D. G. & Goncharov, A. F. Effect of mass disorder on the lattice thermal conductivity of MgO periclase under pressure. *Sci. Rep.* **3**, 2400 (2013).

190. Tang, X. & Dong, J.J. Lattice thermal conductivity of MgO at conditions of Earth's interior. *Proc. Natl. Acad. Sci. USA* **107**, 4539-4543 (2010).

191. Ohta, K. *et al.* Lattice thermal conductivity of $MgSiO_3$ perovskite and post-perovskite at the core–mantle boundary. *Earth Planet. Sci. Lett.* **349-350**, 109-115 (2012).

192. Marzotto, E. *et al.* Effect of water on lattice thermal conductivity of ringwoodite and its implications for the thermal evolution of descending slabs. *Geophys. Res. Lett.* **47**, e87607 (2020).

193. Hsieh, W.-P. *et al.* Spin transition of iron in δ-(Al,Fe)OOH induces thermal anomalies in Earth's lower mantle. *Geophys. Res. Lett.* **47**, e87036 (2020).

194. Elalfy, L., Music, D. & Hu, M. First principles investigation of anomalous pressure-dependent thermal conductivity of chalcopyrites. *Materials* **12**, 3491 (2019).

195. Hohensee, G. T., Fellinger, M. R., Trinkle, D. R. & Cahill, D. G. Thermal transport across high-pressure semiconductor-metal transition in Si and $Si_{0.991}Ge_{0.009}$. *Phys. Rev. B* **91**, 205104 (2015).

196. Harish, S. *et al.* Thermal conductivity reduction of crystalline silicon by high-pressure torsion. *Nanoscale Res. Lett.* **9**, 326 (2014).

197. Kuryliuk, V., Nepochatyi, O., Chantrenne, P., Lacroix, D. & Isaiev, M. Thermal conductivity of strained silicon: Molecular dynamics insight and kinetic theory approach. *J. Appl. Phys.* **126**, 055109 (2019).

198. Xie, H. *et al.* Large tunability of lattice thermal conductivity of monolayer silicene via mechanical strain. *Phys. Rev. B* **93**, 075404 (2016).

199. Raeisi, M., Ahmadi, S. & Rajabpour, A. Modulated thermal conductivity of 2D hexagonal boron arsenide: A strain engineering study. *Nanoscale* **11**, 21799-21810 (2019).

200. Yebra, F., Troncoso, J. & Romaní, L. Thermal conductivity measurements for organic liquids at high pressure. *J. Chem. Thermodyn.* **142**, 106005 (2020).
201. Ross, R. G. & Sandberg, O. The thermal conductivity of four solid phases of NH_4F, and a comparison with H_2O. *J. Phys. C: Solid State Phys.* **11**, 667-672 (1978).
202. McWilliams, R. S., Dalton, D. A., Konôpková, Z., Mahmood, M. F. & Goncharov, A. F. Opacity and conductivity measurements in noble gases at conditions of planetary and stellar interiors. *Proc. Natl. Acad. Sci. USA* **112**, 7925-7930 (2015).
203. Xu, J. *et al.* Thermal conductivity and electrical resistivity of solid iron at Earth's core conditions from first principles. *Phys. Rev. Lett.* **121**, 096601 (2018).
204. de Koker, N., Steinle-Neumann, G. & Vlček, V. Electrical resistivity and thermal conductivity of liquid Fe alloys at high P and T, and heat flux in Earth's core. *Proc. Natl. Acad. Sci. USA* **109**, 4070-4073 (2012).
205. Seagle, C. T., Cottrell, E., Fei, Y., Hummer, D. R. & Prakapenka, V. B. Electrical and thermal transport properties of iron and iron-silicon alloy at high pressure. *Geophys. Res. Lett.* **40**, 5377-5381 (2013).
206. Tang, X. & Dong, J. J. Pressure dependence of harmonic and anharmonic lattice dynamics in MgO: A first-principles calculation and implications for lattice thermal conductivity. *Phys. Earth Planet. Inter.* **174**, 33-38 (2009).
207. Goncharov, A. F., Haugen, B. D., Struzhkin, V. V., Beck, P. & Jacobsen, S. D. Radiative conductivity in the Earth's lower mantle. *Nature* **456**, 231-234 (2008).
208. Goncharov, A. F., Struzhkin, V. V. & Jacobsen, S. D. Reduced radiative conductivity of low-spin (Mg,Fe)O in the lower mantle. *Science* **312**, 1205-1208 (2006).
209. Lobanov, S. S., Holtgrewe, N., Lin, J.-F. & Goncharov, A. F. Radiative conductivity and abundance of post-perovskite in the lowermost mantle. *Earth Planet. Sci. Lett.* **479**, 43-49 (2017).
210. Lobanov, S. S. *et al.* Blocked radiative heat transport in the hot pyrolitic lower mantle. *Earth Planet. Sci. Lett.* **537**, 116176 (2020).
211. Stackhouse, S., Stixrude, L. & Karki, B. B. Thermal conductivity of periclase (MgO) from first principles. *Phys. Rev. Lett.* **104**, 208501 (2010).
212. de Koker, N. Thermal conductivity of MgO periclase at high pressure: Implications for the D″ region. *Earth Planet. Sci. Lett.* **292**, 392-398 (2010).
213. Goncharov, A. F. *et al.* Experimental study of thermal conductivity at high pressures: Implications for the deep Earth's interior. *Phys. Earth Planet. Inter.* **247**, 11-16 (2015).
214. Yagi, T. *et al.* Thermal diffusivity measurement in a diamond anvil cell using a light pulse thermoreflectance technique. *Meas. Sci. Technol.* **22**, 024011, (2010).
215. Chang, Y.-Y., Hsieh, W.-P., Tan, E. & Chen, J. Hydration-reduced lattice thermal conductivity of olivine in Earth's upper mantle. *Proc. Natl. Acad. Sci. USA* **114**, 4078-4081 (2017).
216. Osako, M. & Ito, E. Thermal diffusivity of $MgSiO_3$ perovskite. *Geophys. Res. Lett.* **18**, 239-242 (1991).
217. Hofmeister, A. M. Mantle values of thermal conductivity and the geotherm from phonon lifetimes. *Science* **283**, 1699-1706 (1999).
218. Hofmeister, A. M. Inference of high thermal transport in the lower mantle from laser-flash experiments and the damped harmonic oscillator model. *Phys. Earth Planet.*

Inter. **170**, 201-206 (2008).
219. Okuda, Y. *et al.* The effect of iron and aluminum incorporation on lattice thermal conductivity of bridgmanite at the Earth's lower mantle. *Earth Planet. Sci. Lett.* **474**, 25-31 (2017).
220. Ohta, K., Yagi, T., Hirose, K. & Ohishi, Y. Thermal conductivity of ferropericlase in the Earth's lower mantle. *Earth Planet. Sci. Lett.* **465**, 29-37 (2017).
221. Haigis, V., Salanne, M. & Jahn, S. Thermal conductivity of MgO, $MgSiO_3$ perovskite and post-perovskite in the Earth's deep mantle. *Earth Planet. Sci. Lett.* **355**, 102-108 (2012).
222. Ammann, M. W. *et al.* Variation of thermal conductivity and heat flux at the Earth's core mantle boundary. *Earth Planet. Sci. Lett.* **390**, 175-185 (2014).
223. Tang, X., Ntam, M. C., Dong, J., Rainey, E. S. G. & Kavner, A. The thermal conductivity of Earth's lower mantle. *Geophys. Res. Lett.* **41**, 2746-2752 (2014).
224. Stackhouse, S., Stixrude, L. & Karki, B. B. First-principles calculations of the lattice thermal conductivity of the lower mantle. *Earth Planet. Sci. Lett.* **427**, 11-17 (2015).
225. Yu, C., Zhang, G., Zhang, Y.-W. & Peng, L.-M. Strain engineering on the thermal conductivity and heat flux of thermoelectric Bi_2Te_3 nanofilm. *Nano Energy* **17**, 104-110 (2015).
226. Yang, X. *et al.* Pressure induced excellent thermoelectric behavior in skutterudites $CoSb_3$ and $IrSb_3$. *Phys. Chem. Chem. Phys.* **21**, 851-858 (2019).
227. Liu, J., Choi, G.-M. & Cahill, D. G. Measurement of the anisotropic thermal conductivity of molybdenum disulfide by the time-resolved magneto-optic Kerr effect. *J. Appl. Phys.* **116**, 233107 (2014).
228. Jo, I., Pettes, M. T., Ou, E., Wu, W. & Shi, L. Basal-plane thermal conductivity of few-layer molybdenum disulfide. *Appl. Phys. Lett.* **104**, 201902 (2014).
229. Sahoo, S., Gaur, A. P. S., Ahmadi, M., Guinel, M. J. F. & Katiyar, R. S. Temperature-dependent Raman studies and thermal conductivity of few-layer MoS_2. *J. Phys. Chem. C* **117**, 9042-9047 (2013).
230. Muratore, C. *et al.* Cross-plane thermal properties of transition metal dichalcogenides. *Appl. Phys. Lett.* **102**, 081604 (2013).
231. Jiang, P., Qian, X., Gu, X. & Yang, R. Probing anisotropic thermal conductivity of transition metal dichalcogenides MX_2 (M = Mo, W and X = S, Se) using time-domain thermoreflectance. *Adv. Mater.* **29**, 1701068 (2017).
232. Wang, X. & Tabarraei, A. Phonon thermal conductivity of monolayer MoS_2. *Appl. Phys. Lett.* **108**, 191905 (2016).
233. Yuan, K., Zhang, X., Li, L. & Tang, D. Effects of tensile strain and finite size on thermal conductivity in monolayer WSe_2. *Phys. Chem. Chem. Phys.* **21**, 468-477 (2019).
234. Broido, D. A., Lindsay, L. & Ward, A. Thermal conductivity of diamond under extreme pressure: A first-principles study. *Phys. Rev. B* **86**, 115203 (2012).
235. Nan, C.-W., Birringer, R., Clarke, D. R. & Gleiter, H. Effective thermal conductivity of particulate composites with interfacial thermal resistance. *J. Appl. Phys.* **81**, 6692-6699 (1997).
236. Shenogin, S., Xue, L., Ozisik, R., Keblinski, P. & Cahill, D. G. Role of thermal boundary resistance on the heat flow in carbon-nanotube composites. *J. Appl. Phys.* **95**, 8136-8144 (2004).

237. Koh, Y. K., Cao, Y., Cahill, D. G. & Jena, D. Heat-transport mechanisms in superlattices. *Adv. Funct. Mater.* **19**, 610-615 (2009).
238. Zhou, Y. *et al.* Thermal characterization of polycrystalline diamond thin film heat spreaders grown on GaN HEMTs. *Appl. Phys. Lett.* **111**, 041901 (2017).
239. Zhou, Y. *et al.* Barrier-layer optimization for enhanced GaN-on-diamond device cooling. *ACS Appl. Mater. Interfaces* **9**, 34416-34422 (2017).
240. Young, D. A. & Maris, H. J. Lattice-dynamical calculation of the Kapitza resistance between fcc lattices. *Phys. Rev. B* **40**, 3685-3693 (1989).
241. Hu, M., Keblinski, P. & Schelling, P. K. Kapitza conductance of silicon-amorphous polyethylene interfaces by molecular dynamics simulations. *Phys. Rev. B* **79**, 104305 (2009).
242. Ong, Z.-Y. & Pop, E. Molecular dynamics simulation of thermal boundary conductance between carbon nanotubes and SiO_2. *Phys. Rev. B* **81**, 155408 (2010).
243. Wilson, R. B., Apgar, B. A., Hsieh, W.-P., Martin, L. W. & Cahill, D. G. Thermal conductance of strongly bonded metal-oxide interfaces. *Phys. Rev. B* **91**, 115414 (2015).
244. Duffy, T. S. Synchrotron facilities and the study of the Earth's deep interior. *Rep. Prog. Phys.* **68**, 1811-1859 (2005).
245. Shen, G. Y. & Mao, H. K. High-pressure studies with x-rays using diamond anvil cells. *Rep. Prog. Phys.* **80**, 016101 (2016).
246. Lin, J. F., Alp, E. E. & Goncharov, A. F. in *Treatise on Geochemistry (Second Edition)* Vol. 15 (eds Heinrich D. Holland & Karl K. Turekian) 195-211 (Elsevier, 2014).
247. Lay, T., Hernlund, J. & Buffett, B. A. Core–mantle boundary heat flow. *Nat. Geosci.* **1**, 25-32 (2008).
248. Nimmo, F. in *Treatise on Geophysics (Second Edition)* (ed Gerald Schubert) 27-55 (Elsevier, 2015).
249. Mao, J. *et al.* Advances in thermoelectrics. *Adv. Phys.* **67**, 69-147 (2018).
250. Pei, Y., Wang, H. & Snyder, G. J. Band engineering of thermoelectric materials. *Adv. Mater.* **24**, 6125-6135 (2012).
251. Novak, T. G., Kim, K. & Jeon, S. 2D and 3D nanostructuring strategies for thermoelectric materials. *Nanoscale* **11**, 19684-19699 (2019).
252. Ovsyannikov, S. V. *et al.* Giant improvement of thermoelectric power factor of Bi_2Te_3 under pressure. *J. Appl. Phys.* **104**, 053713 (2008).
253. Ovsyannikov, S. V. & Shchennikov, V. V. Pressure-tuned colossal improvement of thermoelectric efficiency of PbTe. *Appl. Phys. Lett.* **90**, 122103 (2007).
254. Ibarra-Hernández, W., Verstraete, M. J. & Raty, J.-Y. Effect of hydrostatic pressure on the thermoelectric properties of Bi_2Te_3. *Phys. Rev. B* **90**, 245204 (2014).
255. Zhang, Y., Hao, S., Zhao, L.-D., Wolverton, C. & Zeng, Z. Pressure induced thermoelectric enhancement in SnSe crystals. *J. Mater. Chem. A* **4**, 12073-12079 (2016).
256. Alsaleh, N. M., Shoko, E. & Schwingenschlögl, U. Pressure-induced conduction band convergence in the thermoelectric ternary chalcogenide $CuBiS_2$. *Phys. Chem. Chem. Phys.* **21**, 662-673 (2019).
257. Chandra Shekar, N. V., Polvani, D. A., Meng, J. F. & Badding, J. V. Improved thermoelectric properties due to electronic topological transition under high pressure. *Physica B: Condens. Matter* **358**, 14-18 (2005).

258. Polvani, D. A., Meng, J. F., Chandra Shekar, N. V., Sharp, J. & Badding, J. V. Large improvement in thermoelectric properties in pressure-tuned *p*-type $Sb_{1.5}Bi_{0.5}Te_3$. *Chem. Mater.* **13**, 2068-2071 (2001).

Acknowledgements

The authors thank Ho-kwang Mao for the encouragement in the technique development and research. Center for High Pressure Science and Technology Advanced Research (Shanghai), Harbin Institute of Technology (Shenzhen), Academia Sinica (Taipei) and the Carnegie Institution for Science (Washington DC) are gratefully acknowledged for support. This work is funded through the National Key R&D Program of China (Grant No. 2018YFA0305900) at HPSTAR and the Basic Research Program of Shenzhen (Grant No. JCYJ20200109112810241) at HIT. W.P.H. acknowledges support from the Academia Sinica and the Ministry of Science and Technology of Taiwan under Contract AS-CDA-106-M02 and 107-2628-M-001-004-MY3 as well as the fellowship from the Foundation for the Advancement of Outstanding Scholarship of Taiwan. The work at Carnegie is supported by the U.S. National Science Foundation (Grant Nos. EAR-1763287 and EAR-2049127).

Author contributions

X.J.C. developed the outline of this work. Y.Z., Z.Y.D. and X.J.C. compiled all data in tables. Z.Y.D. and Y.Z. drew the figures. All authors contributed to the discussion of content and the preparation of the manuscript in collaboration.

Corresponding author

Correspondence to Xiao-Jia Chen.

Ethics declarations

Competing interests

The authors declare no competing interests.